Immediate and long-lasting impacts of the Mt. Pinatubo eruption on ocean oxygen and carbon inventories

Amanda R Fay[1], Galen A McKinley[2], Nicole Suzanne Lovenduski[3], Yassir A. Eddebbar[4], Michael N Levy[5], Matthew C. Long[5], Holly Olivarez[3], and Rea R Rustagi[6]

[1]Lamont-Doherty Earth Observatory, Columbia University
[2]Columbia University and Lamont-Doherty Earth Observatory
[3]University of Colorado Boulder
[4]Scripps Institution of Oceanography, University of California San Diego
[5]National Center for Atmospheric Research (UCAR)
[6]Columbia University

November 21, 2022

Posted on 21 Nov 2022 — CC-BY-NC 4 — https://doi.org/10.1002/essoar.10511826.1 — This a preprint and has not been peer reviewed. Data may be preliminary.

Abstract

Large volcanic eruptions drive significant climate perturbations through major anomalies in radiative fluxes and the resulting widespread cooling of the surface and upper ocean. Recent studies suggest that these eruptions also drive important variability in air-sea carbon and oxygen fluxes. By simulating the Earth system using two initial-condition large ensembles, with and without the aerosol forcing associated with the Mt. Pinatubo eruption in June 1991, we isolate the impact of this event on ocean physical and biogeochemical properties. The Mt. Pinatubo eruption generated significant anomalies in surface fluxes and the ocean interior inventories of heat, oxygen, and carbon. Pinatubo-driven changes persist for multiple years in the upper ocean and permanently modify the ocean's heat, oxygen, and carbon inventories. Positive anomalies in oxygen concentrations emerge immediately post-eruption and penetrate into the deep ocean. In contrast, carbon anomalies intensify in the upper ocean over several years post-eruption, and are largely confined to the upper 150 m. In the tropics and northern high latitudes, the change in oxygen is dominated by surface cooling and subsequent ventilation to mid-depths, while the carbon anomaly is associated with solubility changes and eruption-generated ENSO variability. Our results indicate that Pinatubo does not substantially impact oxygen or carbon in the Southern Ocean; forced signals do not emerge from the large internal variability in this region.

Immediate and long-lasting impacts of the Mt. Pinatubo eruption on ocean oxygen and carbon inventories

Amanda R. Fay[1], Galen A. McKinley[1], Nicole S. Lovenduski[2,3], Yassir Eddebbar[4], Michael N. Levy[5], Matthew C. Long[5], Holly C. Olivarez[3,6], Rea R. Rustagi[1]

[1]Columbia University and Lamont-Doherty Earth Observatory, Palisades, NY, USA
[2]Department of Atmospheric and Oceanic Sciences, University of Colorado, Boulder, CO, USA
[3]Institute of Arctic and Alpine Research, University of Colorado, Boulder, CO, USA
[4]Scripps Institution of Oceanography, University of California San Diego, La Jolla, CA, USA
[5]Climate and Global Dynamics Laboratory, National Center for Atmospheric Research, Boulder, CO, USA
[6]Department of Environmental Studies, University of Colorado, Boulder, CO, USA

Key Points:

- Two initial-condition large ensembles are used to quantify the ocean physical and biogeochemical response to the 1991 eruption of Mt. Pinatubo
- Oxygen is immediately absorbed into the upper ocean and then transits to depth where it permanently increases the interior inventory by 60 Tmol
- Mt Pinatubo generated a temporary increase in the ocean carbon sink; a 0.29±0.14 Pg C yr^{-1} increase in 1992.

Corresponding author: Amanda R. Fay, afay@ldeo.columbia.edu

Abstract

Large volcanic eruptions drive significant climate perturbations through major anomalies in radiative fluxes and the resulting widespread cooling of the surface and upper ocean. Recent studies suggest that these eruptions also drive important variability in air-sea carbon and oxygen fluxes. By simulating the Earth system using two initial-condition large ensembles, with and without the aerosol forcing associated with the Mt. Pinatubo eruption in June 1991, we isolate the impact of this event on ocean physical and biogeochemical properties. The Mt. Pinatubo eruption generated significant anomalies in surface fluxes and the ocean interior inventories of heat, oxygen, and carbon. Pinatubo-driven changes persist for multiple years in the upper ocean and permanently modify the ocean's heat, oxygen, and carbon inventories. Positive anomalies in oxygen concentrations emerge immediately post-eruption and penetrate into the deep ocean. In contrast, carbon anomalies intensify in the upper ocean over several years post-eruption, and are largely confined to the upper 150 m. In the tropics and northern high latitudes, the change in oxygen is dominated by surface cooling and subsequent ventilation to mid-depths, while the carbon anomaly is associated with solubility changes and eruption-generated ENSO variability. Our results indicate that Pinatubo does not substantially impact oxygen or carbon in the Southern Ocean; forced signals do not emerge from the large internal variability in this region.

Plain Language Summary

The eruption of Pinatubo in June of 1991 produced sunlight-reflecting aerosols in the upper atmosphere and led to a cooling of the planet for several years. While the global cooling following the eruption is well documented, the impact of the eruption on the ocean oxygen and carbon budgets has received comparably little attention. As the global ocean oxygen concentration is declining in response to climate change, and as the ocean's continued storage of anthropogenic carbon is critical for the climate system, it is of interest to quantify the effect of the eruption on both oxygen and carbon in the global ocean. Here, we use an Earth system model to simulate the historical evolution of the climate system both with and without the Mt. Pinatubo eruption. By comparing the simulations, we are able to quantify the effect of the eruption on ocean properties. We find that the eruption led to cooler surface ocean temperatures, and increases in the ocean oxygen and carbon concentrations that persisted for many years. Our simulations can also be used to study other Earth system changes caused by the eruption.

1 Introduction

As a result of anthropogenic activities, the global ocean is losing oxygen and gaining carbon. Observations indicate that the ocean's oxygen inventory has declined by about 2% in the 5 decades following 1960 as the upper ocean warms and stratifies [*Ito et al.*, 2017; *Schmidtko et al.*, 2017]. This oxygen loss has major consequences for nutrient cycling, compression of marine ecosystem habitats, and global fisheries [*Keeling et al.*, 2010; *Gruber*, 2011; *Deutsch et al.*, 2015]. Since pre-industrial times, the ocean has absorbed ~170 Pg of anthropogenic carbon from the atmosphere [*Canadell et al.*, 2021], which is beneficial for the mitigation of anthropogenic warming, but harmful to some organisms through the related decline in pH, known as ocean acidification.

These long-term changes in ocean oxygen and carbon are superimposed on large interannual to multi-decadal variability, challenging the attribution of reported trends [*Long et al.*, 2016; *McKinley et al.*, 2016; *Schlunegger et al.*, 2020]. Due to their sensitivity to physical and biogeochemical processes, the oceanic oxygen concentrations and air-sea flux exhibit substantial variability across a range of timescales in observations and models [*Ito et al.*, 2010; *McKinley et al.*, 2003; *Deutsch et al.*, 2011; *Eddebbar et al.*, 2017]. Modeling and observation-based studies suggest that both air-sea carbon dioxide flux and ocean carbon concentrations exhibit variability on interannual to multi-decadal timescales [*Resplandy et al.*, 2015; *DeVries et al.*, 2017; *Gruber et al.*, 2019]. Many studies highlight internal climate processes and modes of variability (e.g., El Niño - Southern Oscillation, North Atlantic Oscillation, Pacific Decadal Oscillation, Southern Annular Mode) as major drivers controlling variations in the fluxes and inventories of global ocean oxygen and carbon [*McKinley et al.*, 2003, 2004; *Lovenduski et al.*, 2007; *Deutsch et al.*, 2011; *Ito and Deutsch*, 2013; *Landschützer et al.*, 2016; *Eddebbar et al.*, 2017; *McKinley et al.*, 2017; *Landschützer et al.*, 2019; *Gruber et al.*, 2019]. Others suggest an important role for externally driven climate perturbations (e.g., volcanic eruptions) in contributing to these variations [*Frölicher et al.*, 2009; *Frölicher et al.*, 2011; *Frölicher et al.*, 2013; *Eddebbar et al.*, 2019; *McKinley et al.*, 2020]. It is critical that we develop a fundamental understanding of the drivers of past ocean oxygen and carbon variability so as to allow for clear interpretation of the observational record and also that we can more confidently predict future change.

Despite their well-known influence on global and regional climate [*Marshall et al.*, 2022] and ocean heat uptake [*Gupta and Marshall*, 2018], the impact of volcanic eruptions on ocean biogeochemistry is not well quantified. The explosive eruption of the Pinatubo stratovolcano in the Philippines on 15 June 1991 was the largest in the last 100 years. The volcanic release of sulfur dioxide and subsequent aerosols interaction in the stratosphere led to a substantial scattering of shortwave irradiance and a major reduction in solar heating at the sea surface, driving persistent global and regional changes in climate [*Dutton and Christy*, 1992; *Marshall et al.*, 2022]. The subsequent cooling effect from eruptions of this magnitude have the potential to cause a dramatic, though temporary, pause in global warming trends [*Robock and Mao*, 1995; *Church et al.*, 2005]. The eruption immediately preceded a boom in ocean observations occurring with the World Ocean Circulation Experiment (WOCE) and Joint Global Ocean Flux Study (JGOFS). Thus, it is possible the impacts from Pinatubo have been imprinted in these observations.

Past studies suggest that volcanic-induced climate perturbations can have a profound influence on the oceanic oxygen and carbon distributions and air-sea fluxes. Using a model ensemble, *Frölicher et al.* [2009] found that volcanic eruptions lead to an increase in interior ocean oxygen concentrations, with volcanic anomalies in oxygen gradually penetrating the top 500 m of the ocean and persisting for several years, but with considerable interannual to decadal variability. However, the small number of ensemble members (3 members) used in their study made regional attribution and process understanding of volcanic effects difficult due to confounding effects of internal (unforced) climate variability. A more recent modeling study leveraged the large number of ensemble members from the Community Earth System Model (CESM) and Geophysical Fluid Dynamics Laboratory model (GFDL) Large Ensembles (LENS) experiments to explore the volcanic effects from eruptions occurring since 1950 [*Eddebbar et al.*, 2019]. They found that tropical eruptions generate strong and spatially decoupled ocean oxygen and carbon uptake, suggesting different processes at play throughout the ocean regions. The simulated oceanic oxygen uptake associated with the eruptions of Agung (1963), El Chichon (1982), and Pinatubo (1991) occurred primarily at mid and high latitudes and acted to reduce the magnitude of global ocean deoxygenation due to anthropogenic warming. This study also showcased strong carbon uptake at lower latitudes associated with an El Niño-like response to tropical eruptions in the tropical Pacific that is common across Earth system models [*McGregor et al.*, 2020]. While the large number of ensemble members substantially reduced the confounding influence of internal variability, the combined effect of various external forcings (anthropogenic greenhouse gases, industrial aerosols, and volcanic aerosols) in this study challenges direct attribution and isolation of volcanic eruption effects on prolonged timescales.

In this study, we conduct numerical experiments that isolate the ocean's response to the volcanic forcing, so as to more clearly assess long-term deoxygenation trends and understand variations in carbon uptake and storage attributable to the Mt. Pinatubo eruption. We quantify the impacts of the Pinatubo eruption on ocean concentrations and air-sea fluxes of oxygen and carbon, and place them into context with anthropogenic forced changes and internally driven climate variability. While this paper is limited in scope to an introduction of the model experiments and the examination of oxygen and carbon impacts in the ocean, scientists throughout the community will find benefit from these runs for understanding the impact of Pinatubo throughout the climate system.

Here, the combined analysis of oxygen and carbon changes presents a unique and complementary perspective on how ocean biogeochemistry and circulation respond to large scale radiative perturbations. Our tool for assessment of the impacts of Pinatubo is a set of large initial condition ensembles of the CESM Large Ensemble experiment, where each ensemble member has different phasing of internal climate variability. The first ensemble is forced with historical and projected future external forcing, while the second ensemble is forced identically with the sole exception that it excludes the aerosols due to the Pinatubo eruption. This experimental protocol permits a clean separation of the climate and biogeochemical impacts of the Pinatubo eruption on the Earth system.

First we will introduce the model setup experiments for this work. In section 3, we evaluate the global mean and spatial patterns of the difference between these two ensembles for SST, oxygen and carbon air–sea exchanges and inventories. We consider these as indicators of the impact of the eruption on the ocean's physical and biogeochemical state. In section 4, we discuss the mechanisms behind these changes, relationships to climate modes, and consider comparisons to observations and previous modeling work on the topic. Thoughts on the direction for future work are also included here. We conclude in section 5 with a summary of our results.

2 Methods

To generate an initial-condition large ensemble, a climate model is run multiple times under identical forcing, but with very small perturbations in initial conditions. These perturbations evolve naturally and amplify rapidly, such that each ensemble member follows a unique climate trajectory through the phase space. The external forcing response, associated with the shared identical external forcing, is isolated in the mean across ensembles. Within the framework of NCAR's Community Earth System Model Large Ensemble (CESM-LE) effort [*Kay et al.*, 2015], we develop a new experiment with 29 members for 1990-2025 that explicitly excludes the forcing from Pinatubo (CESM-LE-NoPin) and isolates the externally forced response due to the volcanic eruption. The forced effect due to Pinatubo is quantified as the difference between the mean of 29 CESM-LE-NoPin ensemble members and the mean of the 29 CESM-LE members from which these were branched off. This forced effect is not directly observable in the real world. Instead, real world observations are akin to a single ensemble member that includes both the forced signal and internal variability [*Deser et al.*, 2012a,b]. As a coupled climate model, each ensemble member of CESM-LE develops its own phasing of internal variability that does not necessarily correspond with the phasing in the real world observations. The spread across the ensemble indicates the potential magnitude of the Earth system response to Pinatubo across multiple realizations of internal variability. Considering both the forced response and the internal spread, we evaluate the near-term and long-term interior ocean carbon and oxygen effects of Pinatubo, and connect these changes to surface flux patterns. Where appropriate, we place the forced changes and ensemble spread into context with observed changes in the ocean.

2.1 The Community Earth System Model

We use the CESM version 1 [CESM1; *Hurrell et al.*, 2013] to conduct our large ensemble simulations. CESM1 consists of atmosphere, ocean, land, and sea ice component models [*Danabasoglu et al.*, 2012; *Lawrence et al.*, 2012; *Hunke and Lipscomb*, 2008; *Holland et al.*, 2012]. The coupled atmospheric model is the Community Atmospheric Model version 5 (CAM5), integrated at nominal 1° horizontal resolution with 30 vertical levels [*Hurrell et al.*, 2013]. Volcanic radiative forcing is incorporated in the CESM LE using the forcing dataset of *Ammann et al.* [2003]. Stratospheric aerosol in CESM1-CAM5 is treated by prescribing a single, zonally averaged species. The prescription consists of a monthly mean mass distributed on a predefined meridional and vertical grid [*Neely III et al.*, 2016]. This aerosol mass is assumed to be comprised of 75% sulfuric acid and 25% water and to have a constant log-normal size distribution.

The ocean physical model, Parallel Ocean Program, version 2 [*Smith et al.*, 2010] has nominal 1° horizontal resolution and 60 vertical levels. Mesoscale eddy transport, diapycnal mixing, and mixed layer restratification by submesoscale eddies are parameterized with state-of-the-art approaches [*Danabasoglu et al.*, 2020]. The biogeochemical-ecosystem ocean model, known as the Biogeochemical Elemental Cycling (BEC) model, includes multi-nutrient co-limitation on phytoplankton growth and specific phytoplankton functional groups as well as full-depth ocean carbonate system thermodynamics, sea-to-air O_2 and CO_2 fluxes, and a dynamic iron cycle [*Moore et al.*, 2013]. The biogeochemical-ecosystem model compares favorably to observations, though there are some important biases, including weak Southern Ocean CO_2 uptake [*Long et al.*, 2013].

2.2 CESM No Pinatubo experiment (CESM-LE-NoPin)

The CESM-LE-NoPin setup is identical to the CESM-LE setup, but excludes the effect of the eruption by adjusting the volcanic aerosol mass mixing ratio within the model. Specifically, the volcanic aerosol mass mixing ratio values in CESM-LE-NoPin for January 1991 to December 1995 were replaced with values from January 1986 to December 1990 to simulate a time without impact from volcanic eruptions. Since Pinatubo was the dominant climatically important volcano during this period, we attribute the resulting climatic and ocean biogeochemical changes to Pinatubo. With this single change in the model setup, we are capturing effects attributable to the physical climate anomalies, however the methodology utilized in this model set up does not consider impacts from volcanic dust deposition on biomass production or other secondary feedbacks on the ocean from volcanic eruptions [*Hamme et al.*, 2010].

Conceptually, the CESM-LE-NoPin ensemble can be thought of as multiple realizations from a “control" climate that did not experience Pinatubo, while the original CESM-LE can be thought of as an “experiment” where each realization, or ensemble member, includes the eruption. We ran the 29 ensemble members of CESM-LE and CESM-LE-NoPin on the same supercomputer (NCAR Cheyenne) to avoid differences in output generated by machine and compiler changes; the original CESM-LE was run on NCAR’s Yellowstone machine.

2.3 Statistical analysis

We present Pinatubo-driven anomalies throughout the manuscript, where anomalies represent the difference between the CESM-LE and the CESM-LE-NoPin output. We quantify the forced impact of the eruption as the difference between the CESM-LE and CESM-LE-NoPin ensemble means (X). The internal variability is defined as the standard deviation (σ) across the ensemble members (CESM-LE minus CESM-LE-NoPin) at each time step. Analysis is conducted on monthly model output.

The forced impact of the eruption is statistically significant at the 95% confidence level [*Deser et al.*, 2012a] if its ratio of the ensemble mean difference (X) with the internal spread (σ) is greater than 2 divided by the square root of the degrees of freedom (N-1; here N = 29),

$$\frac{X}{\sigma} \geq \frac{2}{\sqrt{N-1}}. \tag{1}$$

When considering annual mean anomalies for the years following the eruption (Figures 4-5), we use July as the first month of each year to ensure symmetry around the peak of ENSO. Consistent with previous work on the topic [*Eddebbar et al.*, 2019], we refer to the 12 months following the eruption as Year 0 [July 1991 -June 1992], and subsequent years as Year 1 [July 1992-June 1993], Year 2 [July 1993-June 1994], etc.

3 Results

Oxygen and carbon in the ocean are sensitive to a number of different physical processes in the climate system. In this section, we briefly describe the eruption-driven changes in ocean temperature, heat content, mixed layer depth, and circulation that are relevant for oxygen and carbon. We then perform a detailed investigation of the oxygen and carbon anomalies driven by Pinatubo.

3.1 Physical response to Pinatubo

The eruption of Pinatubo in June of 1991 drives an immediate reduction in global mean sea surface temperature (SST) followed by a prolonged recovery (Figure 1a). The forced SST anomaly due to Pinatubo reaches a maximum of 0.18°C one year post-eruption, with a statistically significant cooling anomaly persisting for five years post eruption, despite an ensemble spread of ±0.08°C (Figure 1b). Below the sea surface, Pinatubo leads to a substantial heat loss, reaching a maximum of -3.5 x 10^{22} J across the entire water column by mid-1993, with most of this heat loss occurring in the upper 250 meters (Figure 2a,b, 3a). A globally averaged vertical profile Hovmöller plot of the difference of the two ensemble means (CESM-LE minus CESM-LE-NoPin) shows that significant cooling begins in 1992 for the upper ocean, with global-mean anomalies as large as 0.2°C penetrating down to 150m (Figure 3a). Smaller, but still significant, anomalies persist to depths below 1000m. Ocean heat content remains significantly altered by the eruption at the 95% confidence level through the year 2000 for the 250 m inventory and persists longer for full depth inventories (Figure 2b). Below 1000 m, the Pinatubo effect on heat content remains statistically significant for the duration of our experiments that end in 2024 (-2 x 10^{22} J, Figure S1), while the upper 250 m rebounds toward a heat content statistically indistinguishable from CESM-LE-NoPin after 2004 (Figure 2b). While there is some recovery in the two years following the maxima anomaly in OHC, the recovery stops quite abruptly in 1996 for all depths, and only modest changes are seen in the anomalies after that year, specifically at depths below 250m (Figure 2b). Our results show that Pinatubo causes a net heat loss that is not recovered even 3 decades after the eruption, consistent with previous modeling work [*Frölicher et al.*, 2011].

Spatial features of sea surface temperature anomalies show that Pinatubo-driven cooling is concentrated in the tropics in the year immediately following the eruption (Figure 4, left, Year 0). Cooling quickly spreads over much of the surface ocean by Year 1 (1992-93) with significant anomalies, given the spread of internal variability indicated by the model ensemble, throughout much of the Pacific basin (unstippled areas in Figure 4). In Year 1 there is also warming surface temperatures in the eastern equatorial Pacific, indicating the development of an El Niño event (Figure S4). In Year 2 (1993-94), this switches to a forced tendency to La Niña patterns in the equatorial Pacific, while northern hemisphere forced reductions in SST continue. In Year 3 (1994-95), the forced tendency to La Niña is the primary Pinatubo-driven cooling signal that persists. By Year 4 (1995-96), the forced surface cooling has largely dissipated, with internal variability masking any significant signal in the anomalies. Throughout the first 5 years post eruption (Year 0-4), no statistically significant cooling is simulated in the Southern Ocean. The Pacific sector of the Southern Ocean shows the strongest forced signal anomalies, although not emerging from the spread of internal variability, with warming during Year 0 and 1 followed by a cooling in subsequent years. These spatial maps indicate that the global-mean evolution of temperatures (Figure 3a) is initially dominated by the Northern extratropics and then by a multi-year tendency to La Niña conditions in the equatorial Pacific.

Significant forced changes in maximum mixed layer depths (maxMLD) are spatially patchy, but do occur in extratropical locations important to upper and deep ocean ventilation (Figure 4, right). In the North Atlantic subpolar region across Years 0-4, there are some patches of significant forced maxMLD increases, particularly in the eastern gyre and in the Labrador and Irminger Seas. In the North Pacific, mode water regions experience significant forced increase in maxMLD in Year 0 and 1, and some forced decline in Year 4. Only weak forced change in maxMLD anomalies occur in scattered locations throughout the Southern Ocean.

3.2 Oxygen and carbon response to Pinatubo

The physical changes in temperature and circulation following Pinatubo are accompanied by pronounced changes in carbon and oxygen distributions and fluxes (Figure 1). The forced oxygen flux anomaly peaks at 42 Tmol yr^{-1} in 1992, with an ensemble spread (σ) of ±31.5 Tmol yr^{-1}. The forced carbon flux anomaly reaches 0.29 Pg C yr^{-1} in 1992, with an ensemble spread ± 0.14 Pg C yr^{-1}. The ensemble mean anomaly in O_2 and CO_2 flux is robust at the 95% confidence level with the forced response of these fluxes persisting through 1996 (Figure 1d,f). The global mean fluxes are large initially after the eruption due to the cooling of the surface ocean, but then the increased uptake weakens and rebounds to a significant forced reduction in the flux in years 1994-6 as cooling tapers off (Figure 1, left column).

Oxygen and carbon inventory in the top 1000 m for both ensembles illustrate significant perturbations amid a backdrop of decreasing and increasing long-term trends, respectively (Figure 2c,e). The oxygen inventory time series reflects the global deoxygenation trend, and a clear divergence between the ensemble means of the CESM-LE and CESM-LE-NoPin experiments (Figure 2c). The anomalous oxygen uptake by the oceans immediately following the eruption (Figure 1c,d) causes an increase in the O_2 content that is strong enough to temporarily counteract the effects of ocean deoxygenation. This pause in the deoxygenation trend extends though 1995 before the decline resumes (Figure 2c).

There are significant Pinatubo-driven oxygen inventory anomalies for both the upper and deep ocean, with positive anomalies (increased oxygen content with the eruption) in the upper ocean through 1998 (Figure 2d) and lagged changes for the full depth inventory extending for the entire 35 years of this experiment (Figure 2d, Figure S2). Post eruption, oxygen is immediately absorbed into the upper ocean and then transits to depth quickly where it permanently increases the interior inventory by 60 Tmol (Figure 2d). Globally averaged oxygen concentrations increase by as much as 1 mmol m^{-3} in the upper ocean following the eruption, reaching to depths of 250 m in early 1992 and subsequently spreading through the upper kilometer in 1994-1996 (Figure 3b). Anomalies then become insignificant for the global-averaged upper ocean above 250 m, but anomalies at depths greater than 250 m persist for the entire length of the simulation (Figure 3b, S3).

Pinatubo-driven anomalies in oxygen inventory exhibit large spatiotemporal variability across the ocean (Figure 5, left). The oxygen inventory of the upper 1000 m displays ±2 mol m^{-2} anomalies in the Northern hemisphere and the tropics in Years 1-3; anomalies in the Southern Ocean do not emerge until Years 3-4 and are concentrated in the Pacific sector (Figure 5, left). Positive anomalies, indicating greater depth-integrated oxygen due to Pinatubo, emerge first in the western boundary current regions of both the North Pacific and Atlantic basins in Year 1 post eruption, and traverse across the basin with time. In the North Atlantic, subpolar anomalies strengthen from Year 1 to Year 4, concurrent with cool SST anomalies and deeper mixed layer depths in that region (Figure 4). In the North Pacific, increased oxygen inventory is also linked with cool SST and deeper maxMLD anomalies (Figure 5, Figure 4). The positive anomalies in the North Pacific have only made it half way across the basin by Year 4, but the positive anomalies continue in that same trajectory in Years 5-9 (not shown). In these extratropical regions, Pinatubo-driven cooling, maxMLD deepening, and increased oxygen inventories are consistent with enhanced ventilation. The small regions exhibiting Pinatubo-driven maxMLD deepening correspond to critically important regions for upper ocean oxygenation [*van Aken et al.*, 2011; *Deutsch et al.*, 2006] and drive significant anomalies in the global mean oxygen inventory (Figure 2d, 3b).

Anomalous oxygen due to Pinatubo enters the ocean most quickly in the tropical Indian and Pacific, and quickly penetrates into and below the mixed layer in these basins (Figure 6, Figure S7-S8). The largest averaged anomalies are found in the North Pacific basin, exceeding 2 mmol m^{-3} for the regional-average anomaly in the upper ocean by two years post eruption (Figure 6). In all basins, Pinatubo-driven upper ocean oxygen anomalies exhibit seasonality, consistent with intermittent ventilation in wintertime (Figure 6). Anomalies in the North Pacific persist between 100-250m for over a decade. In the North Atlantic, winter of Year 1 (1992-1993) experiences a ventilation anomaly that also causes anomalies greater than 2 mmol/m^3 between 100 and 250m. For multiple years post eruption, wintertime ventilation in the North Atlantic supplies anomalously high oxygen concentrations into the subsurface thermocline ((Figure 6), Figure S5) where oxygen eventually penetrates to depths below 500m (Figure S8). This signal also emerges through a strengthening of the Atlantic MOC during the late 1990s due to this increase in ventilation (Figure S10).

In contrast to the declining oxygen inventory due to ocean warming, Pinatubo-driven anomalies in air-sea CO_2 flux and DIC inventory occur against a background of increasing oceanic CO_2 uptake (Figure 1e) and a steadily increasing DIC inventory (Figure 2e) due to increasing atmospheric CO_2 concentrations prescribed in the modeled atmosphere. The carbon response is associated predominantly with preindustrial carbon, rather than anthropogenic (not shown); all results presented here are for the total carbon. The 0.29 ± 0.14 Pg C yr^{-1} increase in ocean uptake of carbon after the eruption (Figure 1e,f) leads to a modest, but statistically significant increase of the ocean DIC inventory of 0.53 Pg C in 1000m inventory by 1993 (Figure 2f) with anomalies most pronounced in the upper ocean (0.77 Pg C in the upper 250 m, Figure 2f). In contrast to oxygen inventories that increase with the depth of integration (Figure 2d), Pinatubo-driven anomalies in DIC inventory are largest in the upper ocean integrals and decrease with depth. Therefore the anomalies in the shallow depths and full integral become nearly consistent by 1998 (Figure 2f). Figure 3c clearly illustrates that the positive anomalies in global-mean DIC are concentrated in the upper 150 m of the ocean during years 1994-1997 (Figure 3c). The slower equilibration timescale for carbon helps to explain the slower DIC response relative to oxygen. Persistent significant anomalies of DIC due to Pinatubo are not detected at depths below 250 m in the global-mean profile, but there are short-lived forced oscillations between significant positive and negative anomalies of smaller magnitude.

Similar to oxygen, we find that Pinatubo-driven DIC anomalies exhibit spatial heterogeneity. For dissolved inorganic carbon inventory, we focus on the upper 250m (Figure 5) where the global mean profiles indicate the largest forced response (Figure 3c). Pinatubo's forced excitement of an El Niño event followed by a La Niña event (Figure S4) is expressed in the upper ocean DIC inventory; the Eastern (Western) Equatorial Pacific exhibits lower (elevated) DIC inventories one year post-eruption, while anomalously high DIC inventories can be found in the Eastern Equatorial Pacific during Years 2-3 post-eruption (Figure 5). In the extratropics, from Years 1-3, particularly in the North, there are also forced increases in the upper ocean DIC content. This is consistent with increased solubility due to lower annual mean SST in these regions, particularly in Years 1 and 2 (Figure 4, left), that supports increased CO_2 fluxes across the air-sea interface (Figure S6).

The strongest positive forced anomalies in the upper ocean DIC inventory occur in the northern and tropical Pacific and tropical Indian, with some significant increase in the south Pacific as well (Figure 7, Figure S7). In the tropical Pacific, circulation anomalies associated with ENSO modify the depth of the thermocline, generating opposite-signed anomalies with depth; the Pinatubo-driven El Niño event leads to decreased DIC in the upper 100 m, while the subsequent La Niña event produces $\sim>3$ mmol m^{-3} increases in upper ocean DIC concentrations (Figure 7). In the tropical Indian, thermocline oscillations also play a role in the inventory anomalies (Figure 7). In the Northern extratropics, upper ocean DIC anomalies occur several years after the eruption (Figure 7). Unlike oxygen, the additional Pinatubo DIC is concentrated in the upper 100 m and generally does not penetrate to depth (Figure S9). The exception to this is in the tropical Atlantic which shows a positive DIC anomaly reaching down to below 250m by 1998 (Figure S9). Since our division of the regions is made at 30°N, this feature is most likely mode waters that are circulating in the upper subtropical gyre across the 30°N boundary. The positive anomaly persists throughout the length of the simulation at depths between 200 and 400m (Figure S9). In the South Pacific south of 30°S, there are modest positive forced anomalies in DIC above 200m in 1993-1996 (Year 2-4) but the other sectors of the Southern Ocean do not show a similar signal (Figure 7).

Despite clear forced signals in the upper ocean inventories of oxygen and carbon, forced signals in air-sea fluxes are difficult to discern with our model ensemble size (Figure S5-S6). Even with large signals in some regions, forced signals cannot be identified because of the large magnitude of internal variability in the fluxes (equation 1). Focusing on DJF-only fluxes (Figure S5-S6, right) to avoid seasonal cancellation of the signal, does allow for a forced signal to emerge in a few spots (eastern North Atlantic in Year 1 and 3), but on the whole does not allow a forced signal to be identified throughout much of the surface ocean. Inventories are integrated quantities that damp local internal variability, and allow forced signals to more clearly emerge (Figure 1- 3).

Though the flux signals are not statistically identifiable as a forced response at the grid-scale, they do indicate a tendency for increased air-sea exchange of oxygen in North Pacific mode waters in Year 0 and 1 and in the North Atlantic subpolar gyre in Year 2-4 (Figure S5).

DJF anomalies are stronger than annual means in the north, consistent with ventilation being dominantly a wintertime phenomena. For carbon, the strongest annual mean anomalies occur in Year 1 (negative, increased uptake/less efflux with eruption) and in Year 3 and 4 (positive, reduced uptake/increase efflux with eruption) in the equatorial Pacific, consistent with ENSO variability (Figure S6). In DJF, there are some patches of significant flux anomalies at subtropical and subpolar latitudes that are mostly negative in Years 0-1 (indicating increased carbon uptake) and then are increasingly positive. These maps support the result that the ocean initially took up more carbon, but then the forced response involved a transition to a state with a reduced sink.

4 Discussion

4.1 Physical changes with Pinatubo

Our experiments with the CESM Large Ensemble allow precise separation of the physical impacts of Pinatubo and their spatio-temporal evolution in the presence of internal variability. Consistent with long-standing knowledge [*Church et al.*, 2005; *Gleckler et al.*, 2006a,b; *Stenchikov et al.*, 2009; *Eddebbar et al.*, 2019; *Marshall et al.*, 2022], we find that Pinatubo's eruption caused widespread global cooling, including spatially distinct reductions in SST, localized increases in maximum mixed layer depths and negative anomalies in upper ocean heat content. The forced surface cooling response, reaching a maximum of 0.18°C, is comparable to observations. NOAA's Optimum Interpolation Sea Surface Temperature (OISST) climate data record shows a global mean SST cooling of 0.12°C with a four year recovery time to return to pre-eruption global mean temperatures [*Reynolds et al.*, 2007].

The eruption of Pinatubo generates ENSO variability in CESM (Figure S4). A forced tendency to El Niño-like conditions emerges about one year after the eruption and is followed by La Niña-like conditions in subsequent years (Figure S4). Over half, or 15 members, of the CESM-LE members develop an El Niño event post-eruption 1992/3 (DJF), and all of those members develop a strong La Niña event in 1994/5 (DJF). In contrast, only 7 of the CESM-LE-NoPin ensemble members develop El Niños in 1992/3, with 6 of them developing a La Niña event in 1994/5. The significant ENSO response to the Pinatubo eruption in CESM-LE is consistent with other model experiments and paleoproxies that report the emergence of El Niño event in the year following a tropical eruption [*Brad Adams et al.*, 2003; *Ohba et al.*, 2013; *Maher et al.*, 2015; *Stevenson et al.*, 2017; *Predybaylo et al.*, 2017; *Khodri* *et al.*, 2017; *Eddebbar et al.*, 2019]. In the real world, the Pinatubo eruption occurred during a developing positive El Niño - Southern Oscillation (ENSO) index [*NOAA*, 2019]. The limitation of the real world is that it is difficult to cleanly discern the eruption-driven climatic signal from the phasing of internal climate variability and the background warming trend [*Liu et al.*, 2018]. The impacts of ENSO preconditioning prior to a large eruption remain an outstanding challenge for the community studying impacts of volcanic eruptions on the climate system [*Marshall et al.*, 2022; *Swingedouw et al.*, 2017; *Stevenson et al.*, 2017; *Predybaylo et al.*, 2020; *McGregor et al.*, 2020]. Though the extent and mechanisms driving this El Niño-like response in models are still debated [*McGregor et al.*, 2020], the subsequent La Niña-like response to Pinatubo identified in CESM-LE has received little attention.

In contrast to the Pinatubo-driven ENSO response in CESM, the winter (DJF) North Atlantic Oscillation (NAO) index has a significant forced response to the eruption for only about one year during Year 3-4 (1994-1995), while the Southern Annular Mode (SAM) index does not show a significant forced response to the eruption at any time during the model run (Figure S4). This results are consistent with previous modeling studies considering strong volcanic eruptions impact on climate signals which found the tendency for NAO to persist in a positive phase over the first post-eruption decade, beginning in Year 3 post-eruption [*Zanchettin et al.*, 2012]. Likewise for the SAM, *McGraw et al.* [2016] find that in years following major volcanic eruptions there is a tendency to a more positive median SAM index, however internal variability is large and ENSO state can impact this connection.

Additionally, our results show that Pinatubo forces an increase in the Atlantic Meridional Overturning Circulation (AMOC) by 1 Sv (4% of the mean), with individual ensemble members increasing by as much as 5 Sv (20% of the mean) (Figure S10). This is consistent with previous studies indicating that external forcing from volcanoes has an impact on the overturning circulation [*Swingedouw et al.*, 2017; *Fang et al.*, 2021]. The AMOC strengthening found in these CESM anomalies is larger and occurs earlier than that reported by *Zanchettin et al.* [2012]. In their last millennium ensemble results they find an AMOC intensification which culminates roughly one decade after the eruption with anomalies on the order of +0.5 Sv.

4.2 Comparing Pinatubo impacts on carbon and oxygen

Forced carbon and oxygen responses to Pinatubo have quite different spatial patterns (Figure 3,5, S5-S6), but the globally-averaged temporal evolution is reasonably similar. Oxygen is taken up at higher latitudes and deeper horizons than carbon which is primarily taken up at lower latitudes and further up the water column, in agreement with the findings of *Eddebbar et al.* [2019]. Several aspects of the oxygen and carbon systems help to explain these features.

Oxygen has a much faster air-sea equilibration timescale than carbon, supporting larger and more immediate O_2 fluxes following the eruption. In addition, DIC concentrations increase downward while oxygen decreases with depth in the ocean; when cooling drives deeper mixing it brings up water low in O_2, but high in CO_2. Thus, ventilation promotes greater O_2 fluxes, but dampens CO_2 fluxes, hence the larger O_2 uptake than carbon at higher latitudes.

Both carbon and oxygen fluxes experience an immediate forced global increase in ocean uptake and then a few years later, a rebound to a positive anomaly, or less uptake (Figure 1c-f). For both gases, the air-sea gradient, $\Delta pX = pX^{atm}$-pX^{ocean} ($X = O_2$ or CO_2), sets the magnitude of the flux. Any anomalous increase in uptake into the surface ocean raises pX^{ocean} and thus reduces the ΔX such that future fluxes will be damped [*Koch et al.*, 2009; *McKinley et al.*, 2020].

Together, these factors help to explain the larger amplitude anomalies in oxygen fluxes and the deeper penetration of oxygen inventory anomalies. When the surface ocean cools and low oxygen waters are delivered to the surface, oxygen can rapidly be exchanged across the air-sea interface and injected into the deep ocean [*Körtzinger et al.*, 2004; *Atamanchuk et al.*, 2020] (Figure 3,6). The window to the surface ocean then closes and the oxygen anomalies are transported at depth (Figure 3).

In contrast, the immediate cooling with Pinatubo primarily increases the carbon carrying capacity by increasing carbon solubility at the surface. Air-sea carbon exchange slowly adds DIC to the ocean and seasonal mixing and mode water formation spreads this anomaly in the upper 150m. In the tropics, fluxes are modulated by the ENSO cycle, leading to reduced outgassing with the initial post-eruption El Niño, and then additional outgassing with the subsequent La Niña event (Figure S6-S7). The accumulation of DIC in the upper ocean in the first years after the eruption is concentrated in the North Pacific, Indian, and Southern

Ocean (Figure S7). This accumulation acts to create a back pressure on fluxes in Years 2-3 after the eruption (Figure 1e,f, 5, S6).

4.3 Pinatubo impact on oxygen fluxes and inventories

Previous model experiments [*Frölicher et al.*, 2009; *Eddebbar et al.*, 2019] suggest a potentially important role for volcanic eruptions in interrupting ocean deoxygenation and modulating the pronounced interannual-to-decadal variability of the observed ocean oxygen content. The global mean oxygen anomalies forced by Pinatubo, which are isolated in our study, are considerable given current trends measured in the world's ocean. Models predict a decline in the global ocean dissolved oxygen inventory of 1-7% by the year 2100 [*Keeling et al.*, 2010] and estimate that 55 Tmol per year was lost in the 1990s [*Schmidtko et al.*, 2017]. Our model results indicate that the eruption of Pinatubo led to maximum increase in interior oxygen of about 100 Tmol in the top 1000m over the 4 years following the eruption (Figure 2, 3), more than offsetting the expected deoxygenation for the first half of 1990s and leading to a net increase in the oxygen inventory of about 60 Tmol by the end of the simulation.

Another interesting feature of our results is that oxygen anomalies are decoupled in depth from temperature changes in CESM, suggesting processes such as changes in transport or biogeochemical rates as drivers of oxygen uptake in addition to the solubility effects, as previously suggested by [*Eddebbar et al.*, 2019]. For example, temperature anomalies are pronounced in upper 0-100 m, while O_2 anomalies are intensified in the 50-200 m depth range (Figure 3). Oxygen changes are also generally more pronounced at depth below 250m (Figure 2d, Figure S8), which may offer new insights on the response of ocean circulation to volcanic eruptions. The intensification of the AMOC (Figure S10) suggests an increase in the advective supply of oxygen to depth as a result of volcanic eruption in the Atlantic basin. Pronounced cooling and a deepened mixed layer at mid and high latitudes likely lead to intensified oxygen uptake and subduction of newly ventilated waters to depth.

4.4 Mechanisms of air-sea CO_2 flux anomalies with Pinatubo

McKinley et al. [2020] used a simple box model forced with atmospheric pCO_2 and global-mean upper ocean heat content anomalies associated with tropical volcanos to propose a mechanistic explanation for globally integrated air-sea CO_2 flux anomalies since the

1980s. The box model closely replicates (r>0.9) the signals found in ensembles of ocean hindcast models and observation-based pCO_2 products. Based on this evidence, *McKinley et al.* [2020] were the first to propose a significant role for external forcing from Pinatubo in the variability of the ocean carbon sink in the 1990s.

Here, with CESM-LE, we find a significant forced anomaly of 0.29 Pg C yr^{-1} in the 1992 globally-integrated air-sea CO_2 flux forced by Pinatubo in CESM-LE; and individual members of the ensemble have flux anomalies greater than 0.5 Pg C yr^{-1} (Figure 1e,f). CESM-LE also reveals significant spatial structure in the carbon flux and DIC inventory response to the eruption of Pinatubo—the ocean's carbon response to Pinatubo is far from globally uniform (Figure 5,7, S6). In the subtropics and the northern high latitudes, the upper ocean absorbs more carbon, particularly in the subtropics, while ENSO dominates the tropical response (Figure 5, 7). This heterogeneous spatial response is not at all captured in the box model, yet the box model's CO_2 flux anomaly of 0.5 Pg C yr^{-1} is within a factor of two of the CESM-LE forced response. CESM-LE also indicates a similar forced reduction in the ocean carbon sink in 1994-1995 as in the box model. This feature is consistent with more DIC being held in the upper ocean (Figure 5) where it can raise surface ocean pCO_2 and damp the flux (Figure S6) [*McKinley et al.*, 2020].

The evolution of the global-mean ocean heat content (OHC) and global-mean DIC profile (Figure 3) demonstrates the global-mean relationship between upper ocean cooling and DIC content that the box model successfully mimics. The forced change in OHC due to Pinatubo (-3.5 x 10^{22} J) is within the range estimated from observations and other modeling studies [*Church et al.*, 2005; *Gleckler et al.*, 2006a, 2016; *Stenchikov et al.*, 2009; *Eddebbar et al.*, 2019; *DeVries*, 2022]. The OHC anomaly in the 200 m deep box model of *McKinley et al.* [2020] is within a factor of two (-5.5x10^{22} J). As in the box model, the globally averaged behavior of CESM-LE is for the negative OHC anomalies to enhance solubility and allow for enhanced air-sea fluxes to persist for long enough (several years) such that additional carbon can be absorbed in the upper ocean (Figure 3). These CESM-LE experiments demonstrate both this global-mean forced response and allow for deeper understanding of the spatially variable mechanisms forced by Pinatubo.

Another study looking at the external forcing of the Pinatubo eruption on the climate system found a cooling of upper ocean (0-300m) ocean heat content and a subsequent recovery to near zero OHC anomaly by 1996 [*DeVries*, 2022]. However, the models used by

DeVries [2022] utilize only historical SST to represent Pinatubo's external forcing in a steady circulation ocean model. Since these SST anomalies impacted only the top model layer of 10 m depth, the resulting globally-integrated OHC anomaly with Pinatubo (-1x10^{22} J) was substantially smaller than most observational studies [*Church et al.*, 2005; *DeVries*, 2022] and more than 3 times smaller than the forced response estimated here with CESM-LE. Therefore their resulting small externally forced air-sea CO_2 flux response is consistent with the underestimation of globally-integrated upper ocean cooling and the lack of ENSO response or ventilation changes in a model with steady circulation.

CESM-LE demonstrates a clear CO_2 flux anomaly due to Pinatubo in the global integral (Figure 1e,f). But at the local scale, air-sea flux anomalies rarely have a statistically significant forced response (Figure S6). This is because the large internal variability in surface fluxes obscures the forced signal. This finding is directly comparable to the finding that the air-sea CO_2 flux response to COVID-19 emissions reductions is not detectable at the local scale [*Lovenduski et al.*, 2021]. Large internal variability presents a particular challenge to the potential for local flux observations to directly identify climatic signals and argues for continued integration of data into observation-based products from which large-scale signals can be identified [*Fay and McKinley*, 2021; *Fay et al.*, 2021].

CESM-LE indicates that the regional centers for CO_2 flux anomalies due to Pinatubo are primarily in the Northern hemisphere and the tropics, but not in the Southern Ocean (Figure S6). This contrasts to observation-based products that suggest large amplitude decadal variability in Southern Ocean CO_2 fluxes [*Landschützer et al.*, 2015; *Hauck et al.*, 2020; *Bennington et al.*, 2012]. Other mechanisms may be responsible for observed large amplitude Southern Ocean decadal variability [*Gruber et al.*, 2019]. Alternatively, in-situ sampling [*Bakker et al.*, 2016] in the Southern Ocean may have been too sparse to allow for accurate reconstructions [*Gloege et al.*, 2021]. With respect to global mechanisms, CESM-LE indicates that the more vigorous overturning of the 1990s, identified by *DeVries et al.* [2017] as a potential mechanism for ocean carbon sink variability, may have been externally forced by Pinatubo. Better quantifying the magnitude and mechanisms of CO_2 flux decadal variability globally and in the Southern Ocean is an important focal point for current ocean carbon research.

4.5 Future Work

With this analysis, we have only just begun to explore all the insights available regarding the impact of the Pinatubo eruption on the ocean and its biogeochemistry. There is much more to be done in terms of understanding the full extent of Pinatubo's impact on ocean physics and biogeochemistry at global, regional, and local scales.

Integrated column inventories and globally integrated fluxes clearly demonstrate the impact of Pinatubo on ocean oxygen and carbon, but locally, significant forced changes in air-sea fluxes are difficult to identify (Figure S6). Because of the magnitude of internal variability at the surface, future work could expand the number of ensemble members to pinpoint forced changes in surface fluxes.

We highlight here that the Pinatubo effects on ocean biogeochemistry explored in this modeling experiment include the climate impacts of volcanic aerosols on ocean biogeochemistry but do not simulate direct biogeochemical changes associated with increased micronutrient deposition from volcanic ash. Observational studies of smaller eruptions suggest volcanic ash deposition may significantly influence carbon cycling through fertilizing plankton growth at regional scales [*Hamme et al.*, 2010; *Langman et al.*, 2010]. The direct biogeochemical contribution of atmospheric deposition of micronutrients by volcanic ash may have additional and complex effects on carbon and oxygen distributions and inventories. These effects are outside the scope of this work, but are worth examining in follow on experiments.

CESM is just one of many Earth system models that have previously generated large ensembles [*Deser et al.*, 2020]. All models are imperfect representations of the real Earth - for example, this version of CESM underestimates Southern Ocean CO_2 uptake [*Long et al.*, 2013] and we do not know if this bias has a role in the small Southern Ocean impacts from Pinatubo that we find here. It would be of great value to have other modeling centers conduct large ensembles without Pinatubo so that different estimates of forced responses and representation of volcanic aerosol forcings could be compared.

We are currently using the CESM ensembles to investigate the impact of the Pinatubo eruption on hydrographic observations of ocean biogeochemistry [*Olivarez, H.C., Lovenduski, N.S., Eddebbar, Y.A., Fay, A.R., Levy, M., Long, M.C., and McKinley, G.A., The Impact of the Pinatubo Climate Perturbation on Global Ocean Carbon and Biogeochemistry, in preparation for Global Biogeochemical Cycles*]. The bulk of ocean biogeochemical observations that anchor long-term trends were collected in the years following the Pinatubo eruption through the World Ocean Circulation Experiment / Joint Global Ocean Flux Study (WOCE / JGOFS) [*Boyer*, 2018].

Comprehensive model output is available for scientists to investigate other components of the Earth system, such as the atmosphere, sea ice and cryosphere.

5 Conclusions

With two initial-condition large ensembles, we have isolated the impacts of the 1991 eruption of Mt. Pinatubo on ocean physical and biogeochemical properties. Pinatubo forced the ocean to cool to a peak of 0.18^{o}C at the surface and to lose 3.5x10^{22} J of heat. Pinatubo forced an El Ninõ event one year after the eruption, and then La Ninã for the two subsequent years. Upper ocean ventilation increased in key regions, allowing for the penetration of oxygen anomalies to depth. These simulations indicate that the long-term effect of Pinatubo on the ocean heat budget was a loss of 2x10^{22} J that persists for multiple decade.

Associated with these physical changes, the ocean absorbed oxygen and carbon, with peak globally integrated forced flux anomalies in 1992 of 42 Tmol O_2 yr^{-1} and 0.29 Pg C yr^{-1}, respectively. In the tropics and northern high latitudes, the eruption's impact on oxygen is dominated by surface cooling and subsequent ventilation to mid-depths, while the carbon anomaly is associated with solubility changes and eruption-generated ENSO variability. Increased inventories of both gases are found mostly in the tropics and Northern hemisphere, but are very limited in the Southern Ocean. Oxygen anomalies penetrate to the deep ocean, while carbon anomalies remain concentrated in the upper 150 m. For both, full-depth inventories are permanently altered.

Acknowledgments

The authors acknowledge high-performance computing support from Cheyenne (https://doi.org/10.5065/D6RX99HX) provided by NCAR's Computational and Information Systems Laboratory, sponsored by the National Science Foundation (NSF). This material is based upon work supported by the National Center for Atmospheric Research, which is a major facility sponsored by the National Science Foundation under Cooperative Agreement No. 1852977. We are grateful for support from the National Science Foundation (OCE-1948624,

OCE-1948664, OCE-1948728, AGS-2019625, OCE 1948599). We acknowledge the previous work done by the CESM Large Ensemble Community Project.

Open Research: The CESM source code is freely available at http://www2.cesm.ucar.edu. The model outputs described in this paper can be accessed at www.earthsystemgrid.org.

References

Ammann, C. M., G. A. Meehl, W. M. Washington, and C. S. Zender (2003), A monthly and latitudinally varying volcanic forcing dataset in simulations of 20th century climate, *Geophysical Research Letters*, *30*(12), doi:https://doi.org/10.1029/2003GL016875.

Atamanchuk, D., J. Koelling, U. Send, and D. W. R. Wallace (2020), Rapid transfer of oxygen to the deep ocean mediated by bubbles, *Nature Geoscience*, *13*(3), 232–237, doi:10.1038/s41561-020-0532-2.

Bakker, D. C. E., B. Pfeil, C. S. Landa, N. Metzl, K. M. O'Brien, A. Olsen, K. Smith, C. Cosca, S. Harasawa, S. D. Jones, S.-I. Nakaoka, Y. Nojiri, U. Schuster, T. Steinhoff, C. Sweeney, T. Takahashi, B. Tilbrook, C. Wada, R. Wanninkhof, S. R. Alin, C. F. Balestrini, L. Barbero, N. R. Bates, A. A. Bianchi, F. Bonou, J. Boutin, Y. Bozec, E. F. Burger, W.-J. Cai, R. D. Castle, L. Chen, M. Chierici, K. Currie, W. Evans, C. Featherstone, R. A. Feely, A. Fransson, C. Goyet, N. Greenwood, L. Gregor, S. Hankin, N. J. Hardman-Mountford, J. Harlay, J. Hauck, M. Hoppema, M. P. Humphreys, C. W. Hunt, B. Huss, J. S. P. Ibánhez, T. Johannessen, R. Keeling, V. Kitidis, A. Körtzinger, A. Kozyr, E. Krasakopoulou, A. Kuwata, P. Landschützer, S. K. Lauvset, N. Lefèvre, C. Lo Monaco, A. Manke, J. T. Mathis, L. Merlivat, F. J. Millero, P. M. S. Monteiro, D. R. Munro, A. Murata, T. Newberger, A. M. Omar, T. Ono, K. Paterson, D. Pearce, D. Pierrot, L. L. Robbins, S. Saito, J. Salisbury, R. Schlitzer, B. Schneider, R. Schweitzer, R. Sieger, I. Skjelvan, K. F. Sullivan, S. C. Sutherland, A. J. Sutton, K. Tadokoro, M. Telszewski, M. Tuma, S. M. A. C. van Heuven, D. Vandemark, B. Ward, A. J. Watson, and S. Xu (2016), A multi-decade record of high-quality fCO_2 data in version 3 of the Surface Ocean CO_2 Atlas (SOCAT), *Earth Syst. Sci. Data*, *8*(2), 383–413, doi:10.5194/essd-8-383-2016.

Bennington, V., G. A. McKinley, N. R. Urban, and C. P. McDonald (2012), Can spatial heterogeneity explain the perceived imbalance in Lake Superior's carbon budget? A model study, *J. Geophys. Res. Biogeosci.*, *117*(G3), doi:10.1029/2011JG001895.

Boyer, O. B. C. C. H. G. A. G. R. L. A. M. C. P. J. R. D. S. I. S. K. W. M. Z., T.P. (2018), *World Ocean Database 2018*, A. V. Mishonov, Technical Editor, NOAA Atlas NESDIS

87.

Brad Adams, J., M. E. Mann, and C. M. Ammann (2003), Proxy evidence for an el niño-like response to volcanic forcing, *Nature*, *426*(6964), 274–278, doi:10.1038/nature02101.

Canadell, J. G., P. M. S. Monteiro, M. H. Costa, L. C. da Cunha, P. M. Cox, A. V. Eliseev, S. Henson, M. Ishii, S. Jaccard, C. Koven, A. Lohila, P. K. Patra, S. Piao, J. Rogelj, S. Syampungani, S. Zaehle, and K. Zickfeld (2021), Global Carbon and other Biogeochemical Cycles and Feedbacks, *Climate Change 2021: The Physical Science Basis. Contribution of Working Group I to the Sixth Assessment Report of the Intergovernmental Panel on Climate Change [Masson-Delmotte, V., P. Zhai, A. Pirani, S. L. Connors, C. Péan, S. Berger, N. Caud, Y. Chen, L. Goldfarb, M. I. Gomis, M. Huang, K. Leitzell, E. Lonnoy, J.B.R. Matthews, T. K. Maycock, T. Waterfield, O. Yelekçi, R. Yu and B. Zhou (eds.)]*.

Church, J. A., N. J. White, and J. M. Arblaster (2005), Significant decadal-scale impact of volcanic eruptions on sea level and ocean heat content, *Nature*, *438*(7064), 74–77.

Danabasoglu, G., S. C. Bates, B. P. Briegleb, S. R. Jayne, M. Jochum, W. G. Large, S. Peacock, and S. G. Yeager (2012), The CCSM4 Ocean Component, *J. Climate*, *25*(5), 1361–1389.

Danabasoglu, G., J. F. Lamarque, J. Bacmeister, D. A. Bailey, A. K. DuVivier, J. Edwards, L. K. Emmons, J. Fasullo, R. Garcia, A. Gettelman, C. Hannay, M. M. Holland, W. G. Large, P. H. Lauritzen, D. M. Lawrence, J. T. M. Lenaerts, K. Lindsay, W. H. Lipscomb, M. J. Mills, R. Neale, K. W. Oleson, B. Otto-Bliesner, A. S. Phillips, W. Sacks, S. Tilmes, L. van Kampenhout, M. Vertenstein, A. Bertini, J. Dennis, C. Deser, C. Fischer, B. Fox-Kemper, J. E. Kay, D. Kinnison, P. J. Kushner, V. E. Larson, M. C. Long, S. Mickelson, J. K. Moore, E. Nienhouse, L. Polvani, P. J. Rasch, and W. G. Strand (2020), The Community Earth System Model version 2 (CESM2), *J. Adv. Model. Earth Syst.*, *12*(2), e2019MS001,916, doi:10.1029/2019MS001916.

Deser, C., A. Phillips, V. Bourdette, and H. Teng (2012a), Uncertainty in climate change projections: the role of internal variability, *Clim. Dynam.*, *38*(3-4), 527–546, doi:10.1007/s00382-010-0977-x.

Deser, C., R. Knutti, S. Solomon, and A. S. Phillips (2012b), Communication of the role of natural variability in future North American climate, *Nature Clim. Change*, *2*(11), 775–779.

Deser, C., F. Lehner, K. B. Rodgers, T. Ault, T. L. Delworth, P. N. DiNezio, A. Fiore, C. Frankignoul, J. C. Fyfe, D. E. Horton, J. E. Kay, R. Knutti, N. S. Lovenduski, J. Marotzke, K. A. McKinnon, S. Minobe, J. Randerson, J. A. Screen, I. R. Simpson, and M. Ting (2020), Insights from Earth system model initial-condition large ensembles and future prospects, *Nature Clim. Change*, *10*(4), 277–286, doi:10.1038/s41558-020-0731-2.

Deutsch, C., S. Emerson, and L. Thompson (2006), Physical-biological interactions in north pacific oxygen variability, *Journal of Geophysical Research: Oceans*, *111*(C9), doi:https://doi.org/10.1029/2005JC003179.

Deutsch, C., H. Brix, T. Ito, H. Frenzel, and L. Thompson (2011), Climate-forced variability of ocean hypoxia, *Science*, *333*(6040), 336–339, doi:10.1126/science.1202422.

Deutsch, C., A. Ferrel, B. Seibel, H.-O. Pörtner, and R. B. Huey (2015), Climate change tightens a metabolic constraint on marine habitats, *Science*, *348*(6239), 1132–1135, doi:10.1126/science.aaa1605.

DeVries, T. (2022), Atmospheric co_2 and sea surface temperature variability cannot explain recent decadal variability of the ocean co2 sink, *Geophysical Research Letters*, *49*(7), e2021GL096,018, doi:https://doi.org/10.1029/2021GL096018, e2021GL096018 2021GL096018.

DeVries, T., M. Holzer, and F. Primeau (2017), Recent increase in oceanic carbon uptake driven by weaker upper-ocean overturning, *Nature*, *542*(7640), 215–218.

Dutton, E. G., and J. R. Christy (1992), Solar radiative forcing at selected locations and evidence for global lower tropospheric cooling following the eruptions of el chichón and pinatubo, *Geophysical Research Letters*, *19*(23), 2313–2316, doi:https://doi.org/10.1029/92GL02495.

Eddebbar, Y. A., M. C. Long, L. Resplandy, C. Rödenbeck, K. B. Rodgers, M. Manizza, and R. F. Keeling (2017), Impacts of enso on air-sea oxygen exchange: Observations and mechanisms, *Global Biogeochemical Cycles*, *31*(5), 901–921, doi:https://doi.org/10.1002/2017GB005630.

Eddebbar, Y. A., K. B. Rodgers, M. C. Long, A. C. Subramanian, S.-P. Xie, and R. F. Keeling (2019), El Niño–like physical and biogeochemical ocean response to tropical eruptions, *J. Climate*, *32*(9), 2627–2649, doi:10.1175/JCLI-D-18-0458.1.

Fang, S.-W., M. Khodri, C. Timmreck, D. Zanchettin, and J. Jungclaus (2021), Disentangling internal and external contributions to atlantic multidecadal variability over the past millennium, *Geophysical Research Letters*, *48*(23), e2021GL095,990, doi:https:

//doi.org/10.1029/2021GL095990, e2021GL095990 2021GL095990.

Fay, A. R., and G. A. McKinley (2021), Observed regional fluxes to constrain modeled estimates of the ocean carbon sink, *Geophysical Research Letters*, *48*(20), e2021GL095,325, doi:https://doi.org/10.1029/2021GL095325, e2021GL095325 2021GL095325.

Fay, A. R., L. Gregor, P. Landschützer, G. A. McKinley, N. Gruber, M. Gehlen, Y. Iida, G. G. Laruelle, C. Rödenbeck, A. Roobaert, and J. Zeng (2021), Seaflux: harmonization of air–sea co_2 fluxes from surface $p co_2$ data products using a standardized approach, *Earth System Science Data*, *13*(10), 4693–4710, doi:10.5194/essd-13-4693-2021.

Frölicher, T. L., F. Joos, G.-K. Plattner, M. Steinacher, and S. C. Doney (2009), Natural variability and anthropogenic trends in oceanic oxygen in a coupled carbon cycle–climate model ensemble, *Global Biogeochem. Cycles*, *23*(1), doi:10.1029/2008GB003316.

Frölicher, T. L., F. Joos, and C. C. Raible (2011), Sensitivity of atmospheric CO_2 and climate to explosive volcanic eruptions, *Biogeosciences*, *8*(8), 2317–2339, doi:10.5194/bg-8-2317-2011.

Frölicher, T. L., F. Joos, C. C. Raible, and J. L. Sarmiento (2013), Atmospheric CO_2 response to volcanic eruptions: The role of ENSO, season, and variability, *Global Biogeochem. Cycles*, *27*(1), 239–251, doi:https://doi.org/10.1002/gbc.20028.

Gleckler, P. J., K. AchutaRao, J. M. Gregory, B. D. Santer, K. E. Taylor, and T. M. L. Wigley (2006a), Krakatoa lives: The effect of volcanic eruptions on ocean heat content and thermal expansion, *Geophysical Research Letters*, *33*(17), doi:https://doi.org/10.1029/2006GL026771.

Gleckler, P. J., T. M. L. Wigley, B. D. Santer, J. M. Gregory, K. AchutaRao, and K. E. Taylor (2006b), Krakatoa's signature persists in the ocean, *Nature*, *439*(7077), 675–675, doi:10.1038/439675a.

Gleckler, P. J., P. J. Durack, R. J. Stouffer, G. C. Johnson, and C. E. Forest (2016), Industrial-era global ocean heat uptake doubles in recent decades, *Nature Climate Change*, *6*(4), 394–398, doi:10.1038/nclimate2915.

Gloege, L., G. A. McKinley, P. Landschützer, A. R. Fay, T. L. Frölicher, J. C. Fyfe, T. Ilyina, S. Jones, N. S. Lovenduski, K. B. Rodgers, S. Schlunegger, and Y. Takano (2021), Quantifying errors in observationally based estimates of ocean carbon sink variability, *Global Biogeochem. Cycles*, *35*(4), e2020GB006,788, doi:https://doi.org/10.1029/2020GB006788.

Gruber, N. (2011), Warming up, turning sour, losing breath: Ocean biogeochemistry under global change, *Phil. Trans. R. Soc. A.*, *369*(1943), 1980–1996.

Gruber, N., D. Clement, B. R. Carter, R. A. Feely, S. van Heuven, M. Hoppema, M. Ishii, R. M. Key, A. Kozyr, S. K. Lauvset, C. Lo Monaco, J. T. Mathis, A. Murata, A. Olsen, F. F. Perez, C. L. Sabine, T. Tanhua, and R. Wanninkhof (2019), The oceanic sink for anthropogenic co₂ from 1994 to 2007, *Science*, *363*(6432), 1193, doi: 10.1126/science.aau5153.

Gupta, M., and J. Marshall (2018), The climate response to multiple volcanic eruptions mediated by ocean heat uptake: Damping processes and accumulation potential, *Journal of Climate*, *31*(21), 8669 – 8687, doi:10.1175/JCLI-D-17-0703.1.

Hamme, R. C., P. W. Webley, W. R. Crawford, F. A. Whitney, M. D. DeGrandpre, S. R. Emerson, C. C. Eriksen, K. E. Giesbrecht, J. F. R. Gower, M. T. Kavanaugh, M. A. Peña, C. L. Sabine, S. D. Batten, L. A. Coogan, D. S. Grundle, and D. Lockwood (2010), Volcanic ash fuels anomalous plankton bloom in subarctic northeast pacific, *Geophysical Research Letters*, *37*(19), doi:https://doi.org/10.1029/2010GL044629.

Hauck, J., M. Zeising, C. Le Quéré, N. Gruber, D. C. E. Bakker, L. Bopp, T. T. T. Chau, Ö. Gürses, T. Ilyina, P. Landschützer, A. Lenton, L. Resplandy, C. Rödenbeck, J. Schwinger, and R. Séférian (2020), Consistency and challenges in the ocean carbon sink estimate for the Global Carbon Budget, *Front. Mar. Sci.*, *7*, 852, doi:10.3389/fmars.2020.571720.

Holland, M. M., D. A. Bailey, B. P. Briegleb, B. Light, and E. Hunke (2012), Improved sea ice shortwave radiation physics in CCSM4: The impact of melt ponds and aerosols on Arctic sea ice, *J. Climate*, *25*(5), 1413–1430, doi:10.1175/JCLI-D-11-00078.1.

Hunke, E. C., and W. H. Lipscomb (2008), CICE: the Los Alamos sea ice model user's manual, version 4, *Los Alamos Natl. Lab. Tech. Report*, *LA-CC-06-012*.

Hurrell, J. W., M. M. Holland, P. R. Gent, S. Ghan, J. E. Kay, P. J. Kushner, J. F. Lamarque, W. G. Large, D. Lawrence, K. Lindsay, W. H. Lipscomb, M. C. Long, N. Mahowald, D. R. Marsh, R. B. Neale, P. Rasch, S. Vavrus, M. Vertenstein, D. Bader, W. D. Collins, J. J. Hack, J. Kiehl, and S. Marshall (2013), The Community Earth System Model: A Framework for Collaborative Research, *B. Am. Meteorol. Soc.*, *94*(9), 1339–1360, doi: 10.1175/BAMS-D-12-00121.1.

Ito, T., and C. Deutsch (2013), Variability of the oxygen minimum zone in the tropical north pacific during the late twentieth century, *Global Biogeochemical Cycles*, *27*(4), 1119–

1128, doi:https://doi.org/10.1002/2013GB004567.

Ito, T., M. Woloszyn, and M. Mazloff (2010), Anthropogenic carbon dioxide transport in the Southern Ocean driven by Ekman flow, *Nature*, *463*(7277), 80–83.

Ito, T., S. Minobe, M. C. Long, and C. Deutsch (2017), Upper ocean o_2 trends: 1958–2015, *Geophysical Research Letters*, *44*(9), 4214–4223, doi:https://doi.org/10.1002/2017GL073613.

Kay, J. E., C. Deser, A. Phillips, A. Mai, C. Hannay, G. Strand, J. M. Arblaster, S. C. Bates, G. Danabasoglu, J. Edwards, M. Holland, P. Kushner, J. F. Lamarque, D. Lawrence, K. Lindsay, A. Middleton, E. Munoz, R. Neale, K. Oleson, L. Polvani, and M. Vertenstein (2015), The Community Earth System Model (CESM) Large Ensemble project: A community resource for studying climate change in the presence of internal climate variability, *B. Am. Meteorol. Soc.*, *96*(8), 1333–1349, doi:10.1175/BAMS-D-13-00255.1.

Keeling, R. F., A. Körtzinger, and N. Gruber (2010), Ocean Deoxygenation in a Warming World, *Annu. Rev. Mar. Sci.*, *2*(1), 199–229, doi:10.1146/annurev.marine.010908.163855.

Khodri, M., T. Izumo, J. Vialard, S. Janicot, C. Cassou, M. Lengaigne, J. Mignot, G. Gastineau, E. Guilyardi, N. Lebas, A. Robock, and M. J. McPhaden (2017), Tropical explosive volcanic eruptions can trigger el niño by cooling tropical africa, *Nature Communications*, *8*(1), 778, doi:10.1038/s41467-017-00755-6.

Koch, J., G. A. McKinley, V. Bennington, and D. Ullman (2009), Do hurricanes cause significant interannual variability in the air-sea CO_2 flux of the subtropical North Atlantic?, *Geophys. Res. Lett.*, *36*(7), doi:10.1029/2009GL037553.

Körtzinger, A., J. Schimanski, U. Send, and D. Wallace (2004), The Ocean Takes a Deep Breath, *Science*, *306*(5700), 1337, doi:10.1126/science.1102557.

Landschützer, P., N. Gruber, F. A. Haumann, C. Rödenbeck, D. C. E. Bakker, S. van Heuven, M. Hoppema, N. Metzl, C. Sweeney, T. Takahashi, B. Tilbrook, and R. Wanninkhof (2015), The reinvigoration of the Southern Ocean carbon sink, *Science*, *349*(6253), 1221–1224.

Landschützer, P., N. Gruber, and D. C. E. Bakker (2016), Decadal variations and trends of the global ocean carbon sink, *Global Biogeochem. Cycles*, *30*(10), 1396–1417, doi:10.1002/2015GB005359, 2015GB005359.

Landschützer, P., T. Ilyina, and N. S. Lovenduski (2019), Detecting regional modes of variability in observation-based surface ocean pCO_2, *Geophys. Res. Lett.*, *46*(5), 2670–2679, doi:10.1029/2018GL081756.

Langman, O., P. Hanson, S. Carpenter, and Y. Hu (2010), Control of dissolved oxygen in northern temperate lakes over scales ranging from minutes to days, *Aquatic Biology*, *9*(2), 193–202.

Lawrence, D. M., K. W. Oleson, M. G. Flanner, C. G. Fletcher, P. J. Lawrence, S. Levis, S. C. Swenson, and G. B. Bonan (2012), The CCSM4 land simulation, 1850–2005: Assessment of surface climate and new capabilities, *J. Climate*, *25*(7), 2240–2260, doi: 10.1175/JCLI-D-11-00103.1.

Liu, F., C. Xing, L. Sun, B. Wang, D. Chen, and J. Liu (2018), How do tropical, northern hemispheric, and southern hemispheric volcanic eruptions affect enso under different initial ocean conditions?, *Geophysical Research Letters*, *45*(23), 13,041–13,049, doi: https://doi.org/10.1029/2018GL080315.

Long, M. C., K. Lindsay, S. Peacock, J. K. Moore, and S. C. Doney (2013), Twentieth-Century Oceanic Carbon Uptake and Storage in CESM1(BGC), *J. Climate*, *26*(18), 6775–6800, doi:10.1175/JCLI-D-12-00184.1.

Long, M. C., C. Deutsch, and T. Ito (2016), Finding forced trends in oceanic oxygen, *Global Biogeochem. Cycles*, *30*(2), 381–397, doi:10.1002/2015GB005310, 2015GB005310.

Lovenduski, N. S., N. Gruber, S. C. Doney, and I. D. Lima (2007), Enhanced CO_2 outgassing in the Southern Ocean from a positive phase of the Southern Annular Mode, *Global Biogeochem. Cycles*, *21*(2), GB2026, doi:10.1029/2006GB002900.

Lovenduski, N. S., N. C. Swart, A. J. Sutton, J. C. Fyfe, G. A. McKinley, C. Sabine, and N. L. Williams (2021), The ocean carbon response to COVID-related emissions reductions, *Geophys. Res. Lett.*, *48*(6), e2020GL092,263, doi:https://doi.org/10.1029/2020GL092263.

Maher, N., S. McGregor, M. H. England, and A. S. Gupta (2015), Effects of volcanism on tropical variability, *Geophysical Research Letters*, *42*(14), 6024–6033, doi:https://doi.org/10.1002/2015GL064751.

Marshall, L. R., E. C. Maters, A. Schmidt, C. Timmreck, A. Robock, and M. Toohey (2022), Volcanic effects on climate: recent advances and future avenues, *Bulletin of Volcanology*, *84*(5), 54, doi:10.1007/s00445-022-01559-3.

McGraw, M. C., E. A. Barnes, and C. Deser (2016), Reconciling the observed and modeled southern hemisphere circulation response to volcanic eruptions, *Geophysical Research Letters*, *43*(13), 7259–7266, doi:https://doi.org/10.1002/2016GL069835.

McGregor, S., M. Khodri, N. Maher, M. Ohba, F. S. R. Pausata, and S. Stevenson (2020), *The Effect of Strong Volcanic Eruptions on ENSO*, chap. 12, pp. 267–287, American Geophysical Union (AGU), doi:https://doi.org/10.1002/9781119548164.ch12.

McKinley, G. A., M. J. Follows, J. Marshall, and S.-M. Fan (2003), Interannual variability of air-sea o2 fluxes and the determination of co2 sinks using atmospheric o2/n2, *Geophysical Research Letters*, *30*(3), doi:https://doi.org/10.1029/2002GL016044.

McKinley, G. A., M. J. Follows, and J. Marshall (2004), Mechanisms of air-sea CO_2 flux variability in the equatorial Pacific and the North Atlantic, *Global Biogeochem. Cycles*, *18*(2), C07S06, doi:10.1029/2003GB002179.

McKinley, G. A., D. J. Pilcher, A. R. Fay, K. Lindsay, M. C. Long, and N. S. Lovenduski (2016), Timescales for detection of trends in the ocean carbon sink, *Nature*, *530*(7591), 469–472.

McKinley, G. A., A. R. Fay, N. S. Lovenduski, and D. J. Pilcher (2017), Natural variability and anthropogenic trends in the ocean carbon sink, *Annu. Rev. Mar. Sci.*, *9*(1), 125–150, doi:10.1146/annurev-marine-010816-060529.

McKinley, G. A., A. R. Fay, Y. A. Eddebbar, L. Gloege, and N. S. Lovenduski (2020), External forcing explains recent decadal variability of the ocean carbon sink, *AGU Advances*, *1*(2), e2019AV000,149, doi:10.1029/2019AV000149.

Moore, J. K., K. Lindsay, S. C. Doney, M. C. Long, and K. Misumi (2013), Marine ecosystem dynamics and biogeochemical cycling in the Community Earth System Model [CESM1(BGC)]: Comparison of the 1990s with the 2090s under the RCP4.5 and RCP8.5 scenarios, *J. Climate*, *26*(23), 9291–9312, doi:10.1175/JCLI-D-12-00566.1.

Neely III, R. R., A. J. Conley, F. Vitt, and J.-F. Lamarque (2016), A consistent prescription of stratospheric aerosol for both radiation and chemistry in the community earth system model (cesm1), *Geoscientific Model Development*, *9*(7), 2459–2470, doi:10.5194/gmd-9-2459-2016.

NOAA (2019), National Oceanic and Atmospheric Administration.

Ohba, M., H. Shiogama, T. Yokohata, and M. Watanabe (2013), Impact of strong tropical volcanic eruptions on enso simulated in a coupled gcm, *Journal of Climate*, *26*(14), 5169 – 5182, doi:10.1175/JCLI-D-12-00471.1.

Predybaylo, E., G. L. Stenchikov, A. T. Wittenberg, and F. Zeng (2017), Impacts of a pinatubo-size volcanic eruption on enso, *Journal of Geophysical Research: Atmospheres*, *122*(2), 925–947, doi:https://doi.org/10.1002/2016JD025796.

Predybaylo, E., G. Stenchikov, A. T. Wittenberg, and S. Osipov (2020), El niño/southern oscillation response to low-latitude volcanic eruptions depends on ocean pre-conditions and eruption timing, *Communications Earth & Environment*, *1*(1), 12, doi:10.1038/s43247-020-0013-y.

Resplandy, L., R. Séférian, and L. Bopp (2015), Natural variability of CO_2 and O_2 fluxes: What can we learn from centuries-long climate models simulations?, *J. Geophys. Res. Oceans*, *120*(1), 384–404, doi:10.1002/2014JC010463.

Reynolds, R. W., T. M. Smith, C. Liu, D. B. Chelton, K. S. Casey, and M. G. Schlax (2007), Daily high-resolution-blended analyses for sea surface temperature, *Journal of Climate*, *20*(22), 5473 – 5496, doi:10.1175/2007JCLI1824.1.

Robock, A., and J. Mao (1995), The volcanic signal in surface temperature observations, *Journal of Climate*, *8*(5), 1086 – 1103, doi:10.1175/1520-0442(1995)008<1086:TVSIST>2.0.CO;2.

Schlunegger, S., K. B. Rodgers, J. L. Sarmiento, T. Ilyina, J. P. Dunne, Y. Takano, J. R. Christian, M. C. Long, T. L. Frölicher, R. Slater, and F. Lehner (2020), Time of Emergence and Large Ensemble intercomparison for ocean biogeochemical trends, *Global Biogeochem. Cycles*, *34*(8), e2019GB006,453, doi:https://doi.org/10.1029/2019GB006453.

Schmidtko, S., L. Stramma, and M. Visbeck (2017), Decline in global oceanic oxygen content during the past five decades, *Nature*, *542*(7641), 335–339, doi:10.1038/nature21399.

Smith, R., P. Jones, B. Briegleb, F. Bryan, G. Danabasoglu, J. Dennis, J. Dukowicz, C. Eden, B. Fox-Kemper, P. Gent, M. Hecht, S. Jayne, M. Jochum, W. Large, K. Lindsay, M. Maltrud, N. Norton, S. Peacock, M. Vertenstein, and S. Yeager (2010), *The Parallel Ocean Program (POP) Reference Manual*, Los Alamos National Laboratory Tech. Rep. LAUR-10-01853, Los Alamos, NM.

Stenchikov, G., T. L. Delworth, V. Ramaswamy, R. J. Stouffer, A. Wittenberg, and F. Zeng (2009), Volcanic signals in oceans, *Journal of Geophysical Research: Atmospheres*, *114*(D16), doi:https://doi.org/10.1029/2008JD011673.

Stevenson, S., J. T. Fasullo, B. L. Otto-Bliesner, R. A. Tomas, and C. Gao (2017), Role of eruption season in reconciling model and proxy responses to tropical volcanism, *Proceedings of the National Academy of Sciences*, *114*(8), 1822–1826, doi:10.1073/pnas.1612505114.

Swingedouw, D., J. Mignot, P. Ortega, M. Khodri, M. Menegoz, C. Cassou, and V. Hanquiez (2017), Impact of explosive volcanic eruptions on the main climate variability modes, *Global and Planetary Change*, *150*, 24–45, doi:https://doi.org/10.1016/j.gloplacha.2017.01.006.

van Aken, H. M., M. F. de Jong, and I. Yashayaev (2011), Decadal and multi-decadal variability of Labrador Sea Water in the north-western North Atlantic Ocean derived from tracer distributions: Heat budget, ventilation, and advection, *Deep-Sea Res. I*, *58*(5), 505 – 523, doi:https://doi.org/10.1016/j.dsr.2011.02.008.

Zanchettin, D., C. Timmreck, H. F. Graf, A. Rubino, S. Lorenz, K. Lohmann, K. Krüger, and J. H. Jungclaus (2012), Bi-decadal variability excited in the coupled ocean–atmosphere system by strong tropical volcanic eruptions, *Climate Dynamics*, *39*(1), 419–444, doi:10.1007/s00382-011-1167-1.

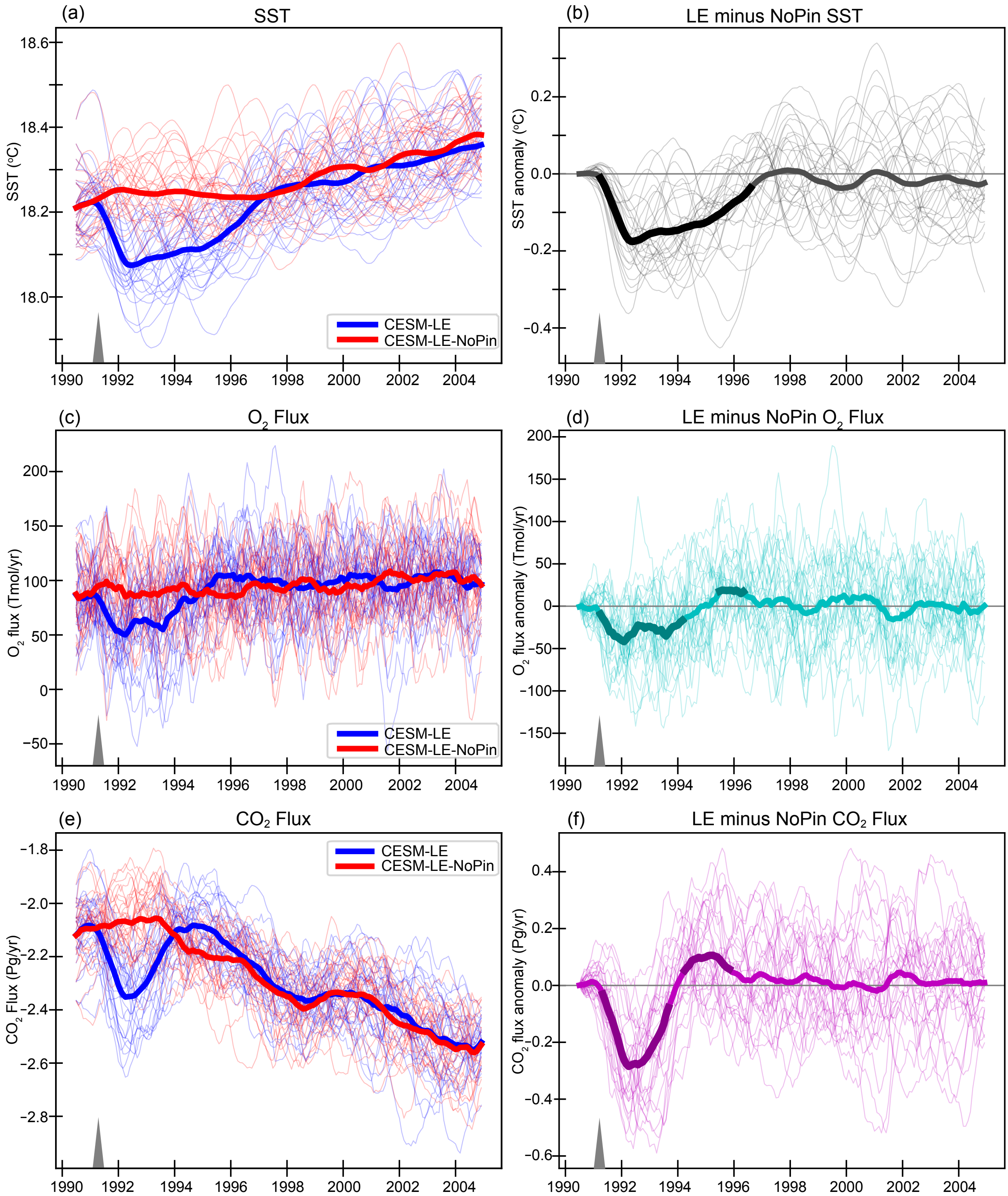

938 **Figure 1.** Left column: CESM-LE (blue) and CESM-LE-NoPin (red) individual members (thin lines) and ensemble mean (thick line) time series for global mean SST (top, degC), Oxygen flux (middle, Tmol/yr), and CO_2 Flux (bottom, Pg/yr) for 1990-2004. Right column: CESM-LE minus CESM-LE-NoPin difference for each variable with thicker line indicating significant difference between the two ensembles at 2σ [*Deser et al.*, 2012a]. Time series are seasonally detrended and smoothed with a 12-month running mean. Gray triangles mark timing of eruption. Full time series through 2025 available in Figure S1.

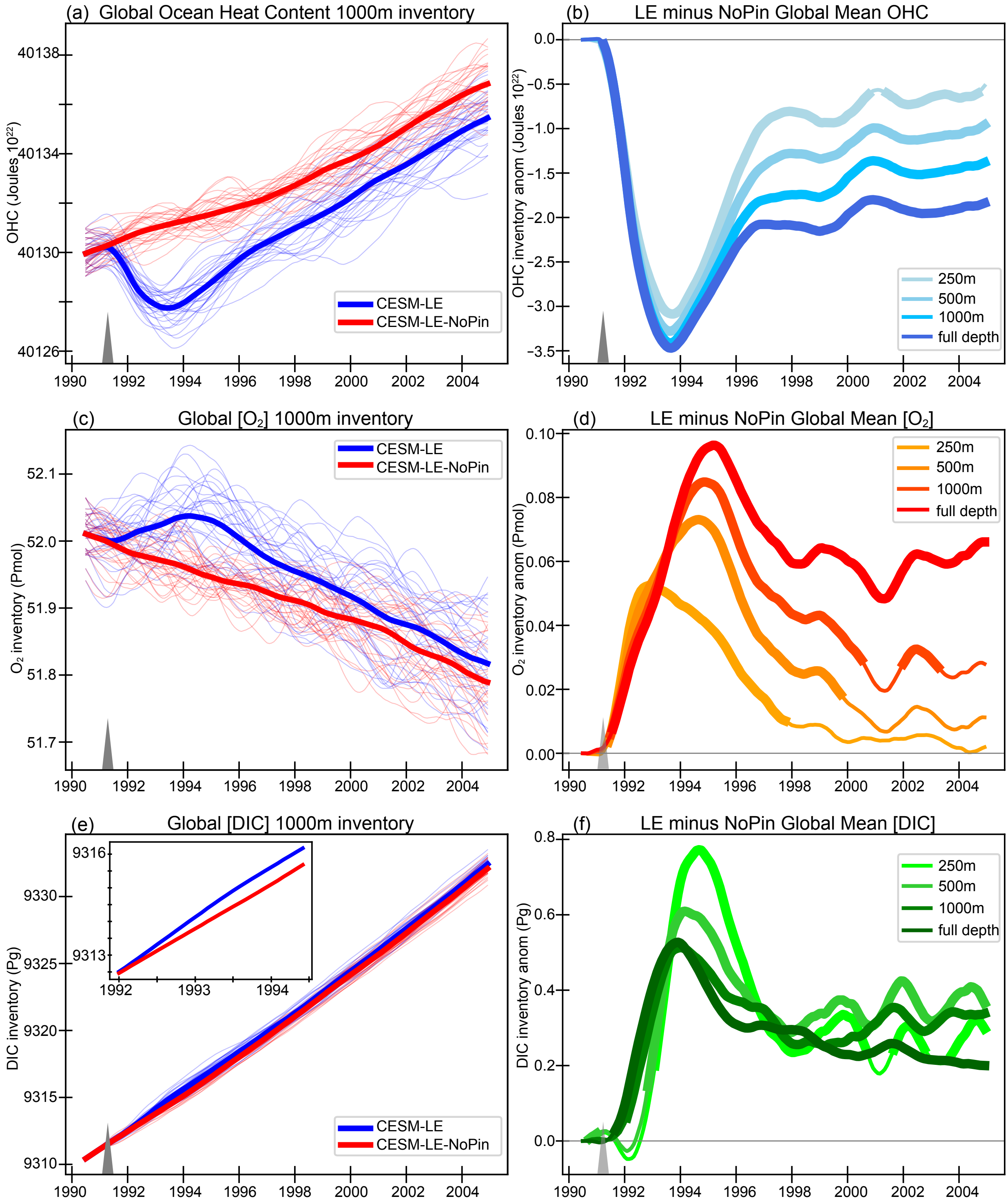

944 **Figure 2.** Left column: CESM-LE (blue) and CESM-LE-NoPin (red) individual members (thin lines) and ensemble mean (thick line) time series for global mean Ocean Heat Content (top, Joules 10^{22}), Oxygen inventory (middle, Pmol), and Dissolved Inorganic Carbon inventory (bottom, Pg) for top 1000m. Inset on DIC inventory (bottom, left) shows a zoomed in ensemble mean time series for 1992-1995 to highlight the difference post eruption. Right column: CESM-LE minus CESM-LE-NoPin inventory difference for each variable with thicker line indicating significant difference between two ensembles at 2σ [*Deser et al.*, 2012a]. Inventory plots include lines for depths 250m, 500m, 1000m and full depth. Time series are seasonally de-trended, smoothed with a 12-month running mean. Gray triangle marks timing of eruption. Full time series through 2025 available in Figure S2.

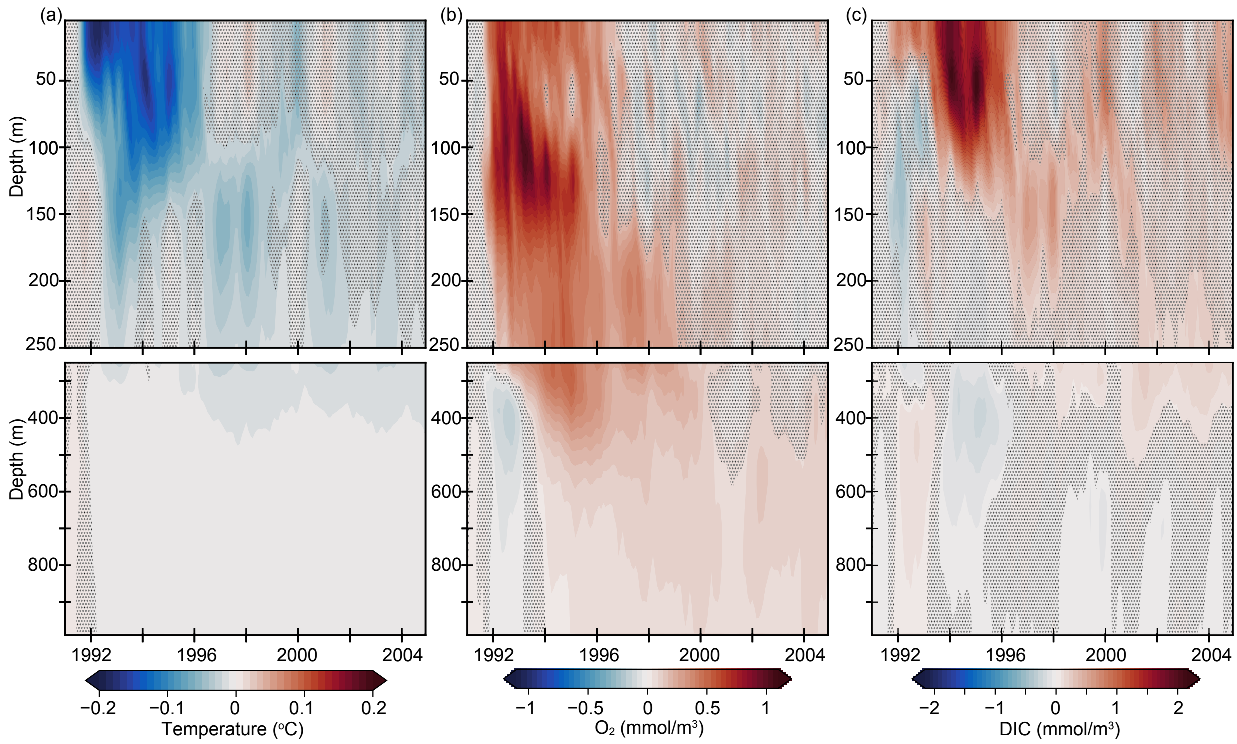

953 **Figure 3.** Globally averaged vertical profile of difference plots (CESM-LE minus CESM-LE-NoPin) for
954 ensemble mean in a) temperature (°C) b) [O_2] (mmol/m^3), and c) [DIC] (mmol/mm^3). Stippling indicates
955 time/depth where differences are not significant at the 95% confidence level [*Deser et al.*, 2012a]. Positive
956 anomalies (warm colors) indicate greater values with the eruption of Pinatubo while negative anomalies (cool
957 colors) indicate lower values with the eruption. Full model time period available in Figure S3.

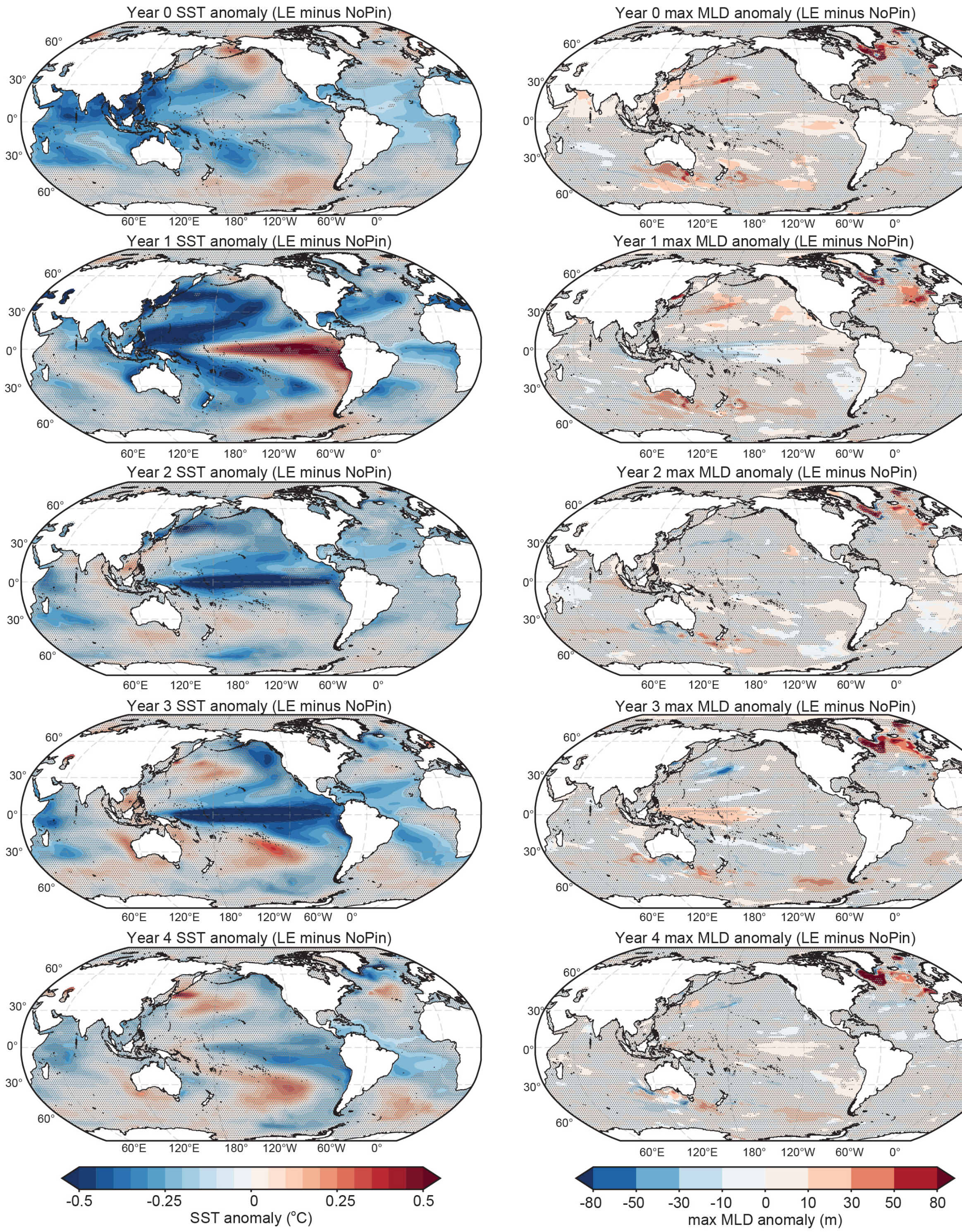

958 **Figure 4.** Evolution of annual mean anomalies (CESM-LE minus CESM-LE-NoPin) sea surface temperature (SST) and maximum mixed layer depth (maxMLD) during the first five years following the June 1991 eruption of Pinatubo: Year 0 (July 1991-June 1992), Year 1 (July 1992-June 1993); Year 2 (July 1993-June 1994); Year 3 (July 1994-June 1995); Year 4 (July 1995-June 1996). SST anomalies are calculated by removing the seasonal cycle and annually averaging over respective months. Positive anomalies (warm colors) indicate warmer temperatures and deeper maximum mixed layer depths with the eruption of Pinatubo. Stippling indicates areas without significant difference between the two ensembles at 2σ [*Deser et al.*, 2012a].

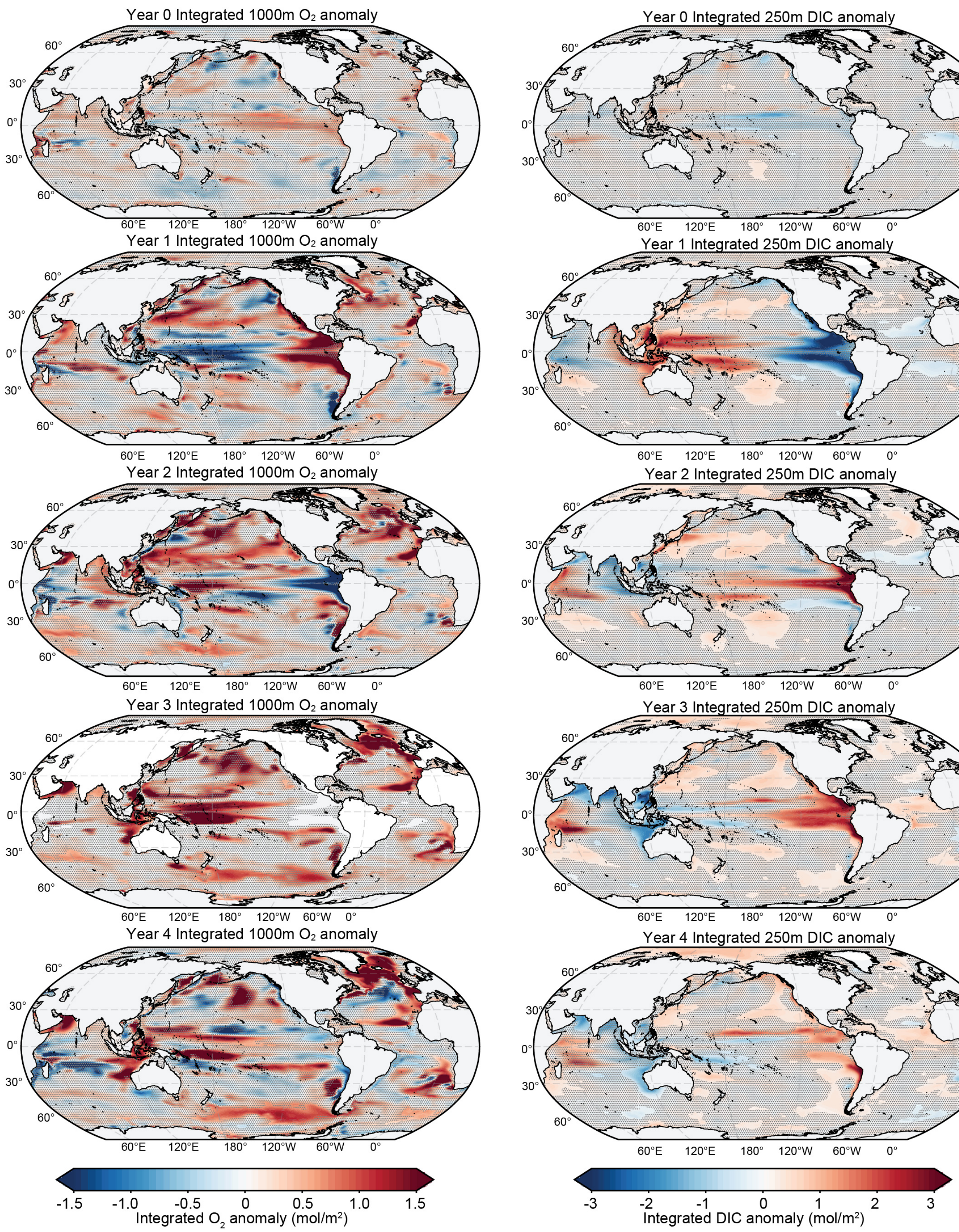

965 **Figure 5.** Evolution of annual mean anomalies (CESM-LE minus CESM-LE-NoPin) depth integrated O_2
966 (top 1000m) and DIC (top 250m) concentrations during the first five years following the June 1991 eruption
967 of Pinatubo: Year 0 (July 1991-June 1992), Year 1 (July 1992-June 1993); Year 2 (July 1993-June 1994);
968 Year 3 (July 1994-June 1995); Year 4 (July 1995-June 1996). Anomalies are calculated by removing the sea-
969 sonal cycle and annually averaging over respective months. Positive anomalies (warm colors) indicate greater
970 depth-integrated O_2 or DIC with the eruption of Pinatubo. Stippling indicates areas without significant
971 difference between the two ensembles at 2σ [*Deser et al.*, 2012a].

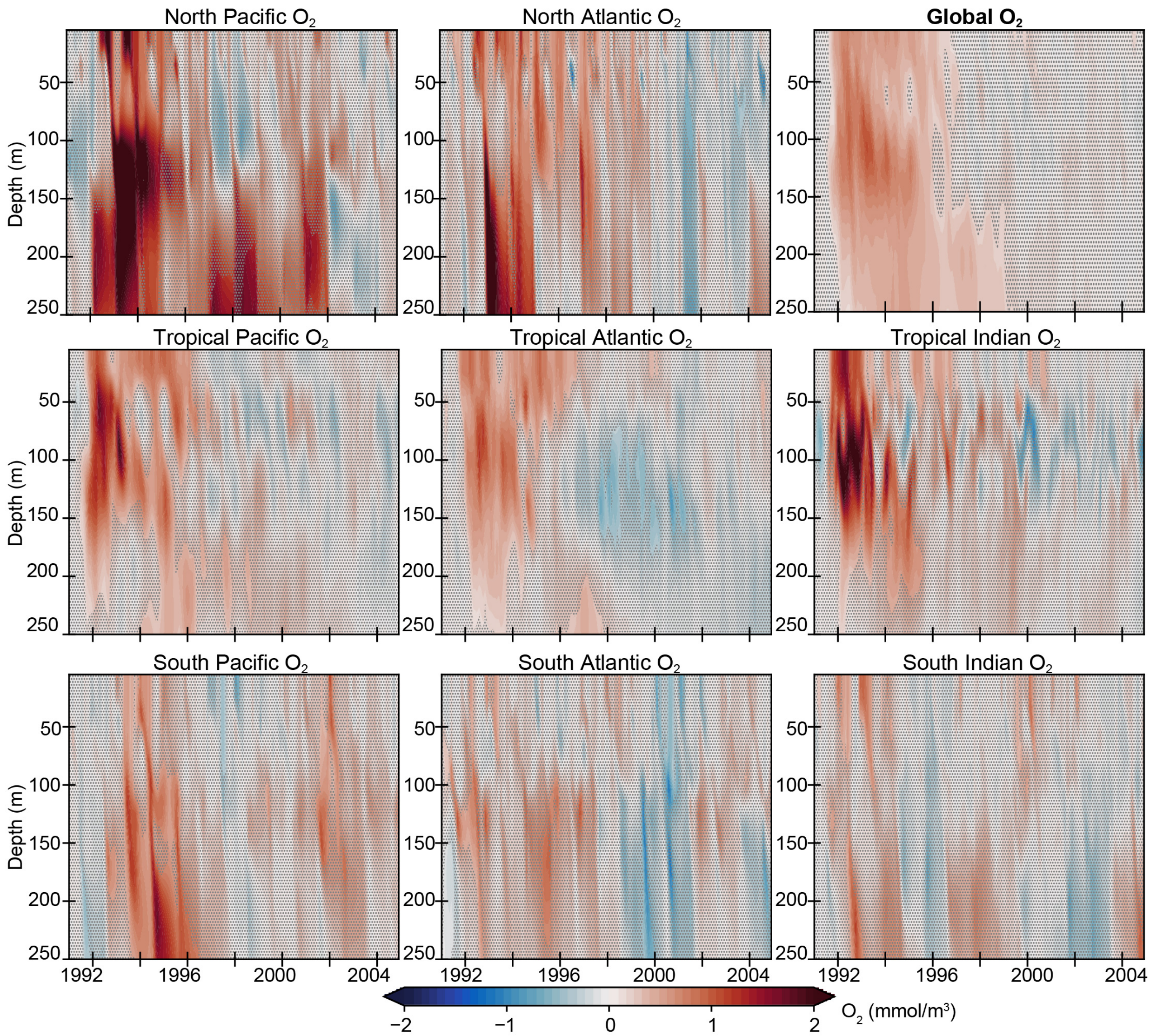

972 **Figure 6.** Regionally averaged vertical profile of difference (CESM-LE minus CESM-LE-NoPin) plots for ensemble mean O_2 inventory (mmol/m^3). Separations are made for the Pacific, Atlantic, and Indian basins into northern (>30°N), tropical (30°N-30°S), and southern sections (<30°S) while the global profile is shown in the top right panel. Stippling indicates time/depth where differences are not significant at the 95% confidence level [*Deser et al.*, 2012a]. Positive anomalies (warm colors) indicate greater oxygen inventory values with the eruption of Pinatubo while negative anomalies (cool colors) indicate lower oxygen with the eruption. Similar plot with depth extending to 1000m is available in Figure S8.

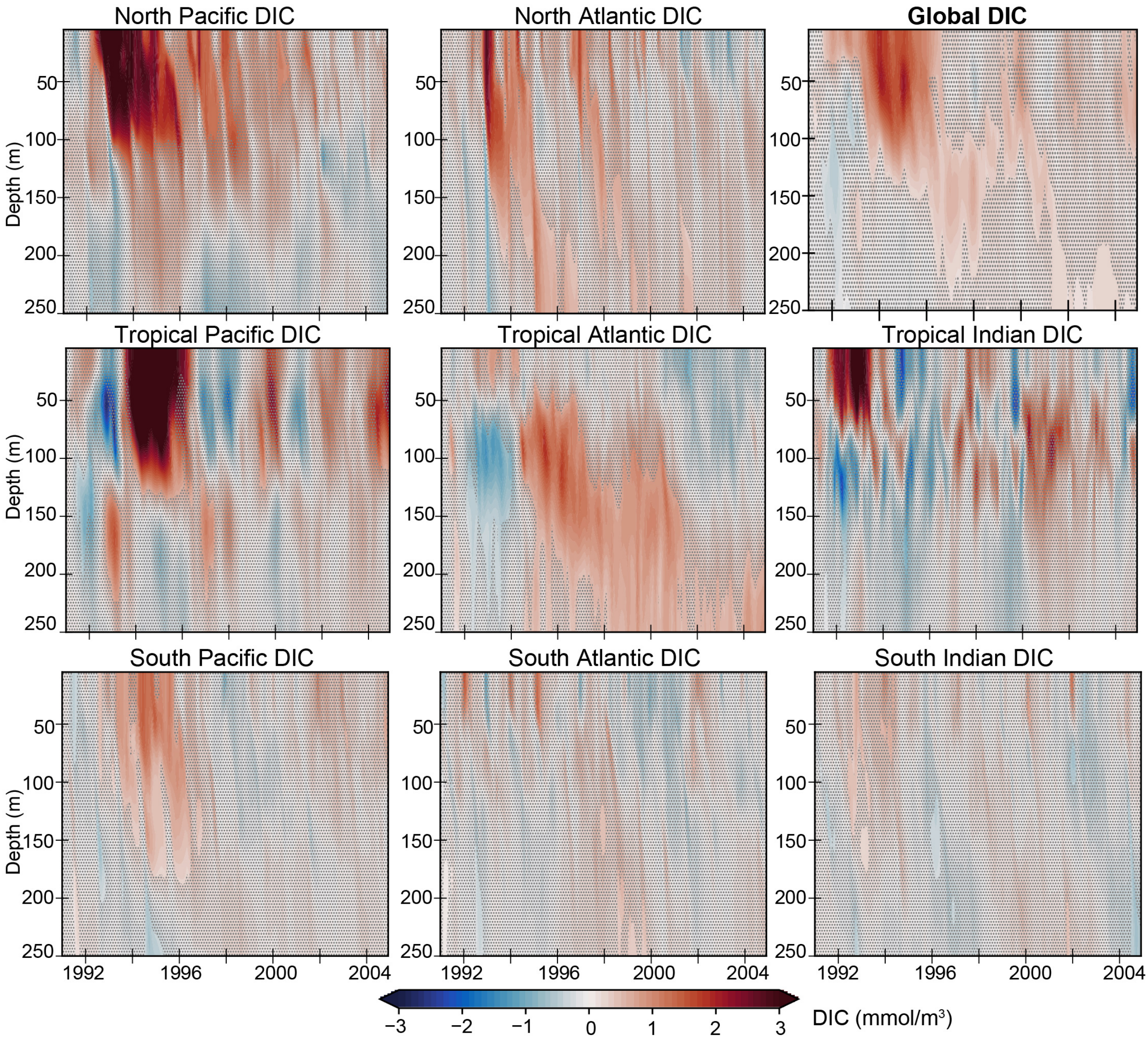

979 **Figure 7.** Regionally averaged vertical profile of difference (CESM-LE minus CESM-LE-NoPin) plots
980 for ensemble mean DIC inventory (mmol/m^3). Separations are made for the Pacific, Atlantic, and Indian
981 basins into northern (>30°N), tropical (30°N-30°S), and southern sections (<30°S) while the global profile
982 is shown in the top right panel. Stippling indicates time/depth where differences are not significant at the
983 95% confidence level [*Deser et al.*, 2012a]. Positive anomalies (warm colors) indicate greater DIC inventory
984 values with the eruption of Pinatubo while negative anomalies (cool colors) indicate lower DIC levels with the
985 eruption. Similar plot with depth extending to 1000m is available in Figure S9.

Supporting Information for "Immediate and long-lasting impacts of the Mt. Pinatubo eruption on ocean oxygen and carbon inventories"

Amanda R. Fay[1], Galen A. McKinley[1], Nicole S. Lovenduski[2,3], Yassir Eddebbar[4], Michael N. Levy[5], Matthew C. Long[5], Holly C. Olivarez[3,6], Rea R. Rustagi[1]

[1]Columbia University and Lamont-Doherty Earth Observatory, Palisades, NY, USA

[2]Department of Atmospheric and Oceanic Sciences, University of Colorado, Boulder, CO, USA

[3]Institute of Arctic and Alpine Research, University of Colorado, Boulder, CO, USA

[4]Scripps Institution of Oceanography, University of California San Diego, La Jolla, CA, USA

[5]Climate and Global Dynamics Laboratory, National Center for Atmospheric Research, Boulder, CO, USA

[6]Department of Environmental Studies, University of Colorado, Boulder, CO, USA

Contents of this file

1. Figures S1 to S11

Introduction This supporting information provides additional figures to support the findings presented in the manuscript. We show the complete time series (1990-2025) for most of the main figures as well as additional information related to climate indices which help with the interpretation of the results.

Corresponding author: A. R. FAY, Columbia University and Lamont-Doherty Earth Observatory, 61 Route W Palisades, NY, 10964 USA (afay@ldeo.columbia.edu)

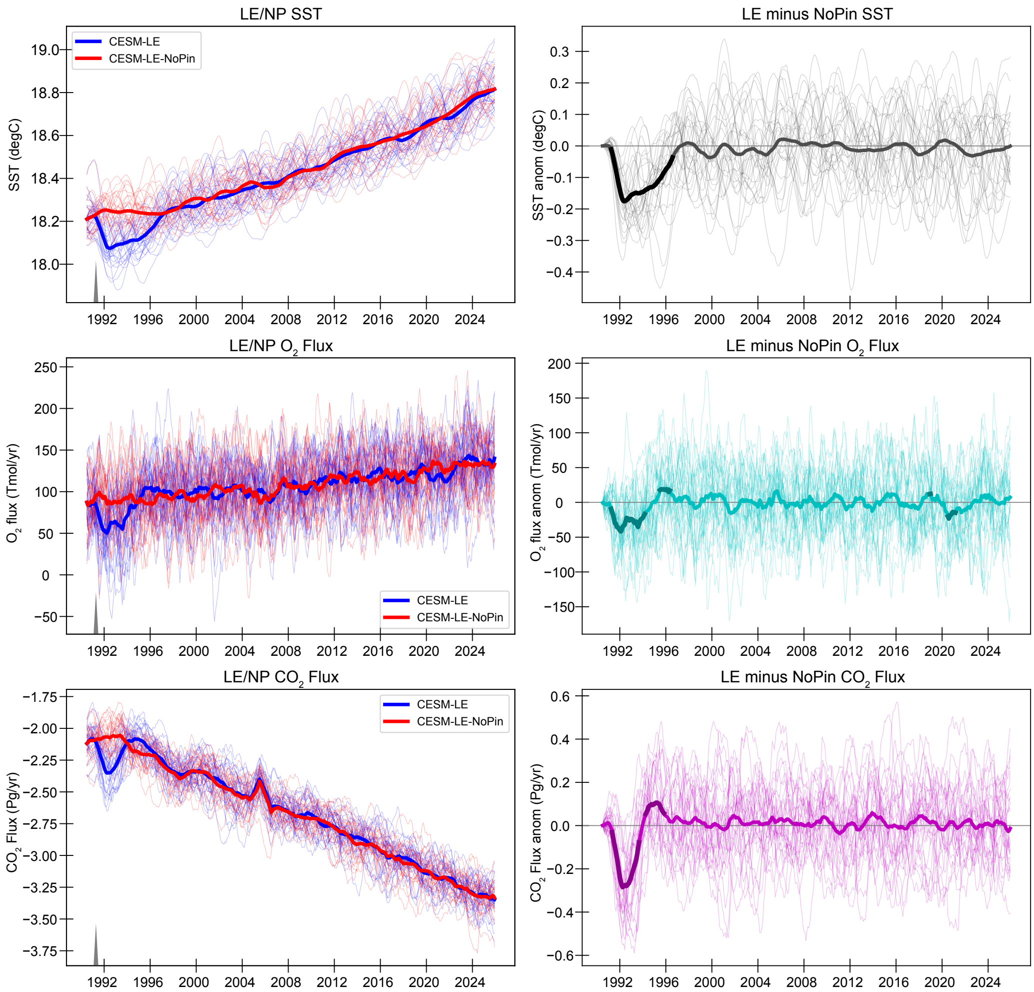

Figure S1. Left column: CESM-LE (blue) and CESM-LE-NoPin (red) individual members (thin lines) and ensemble mean (thick line) time series for global mean SST (black, degC), Oxygen flux (teal, Tmol/yr), and CO_2 Flux (magenta, Pg/yr) for full model time series (1990-2025). Right column: CESM-LE minus CESM-LE-NoPin difference for each variable with thicker line indicating significant difference between two ensembles at 2σ Deser:2012a. Time series are seasonally detrended, smoothed with a 12-month running mean. Gray triangle marks timing of eruption.

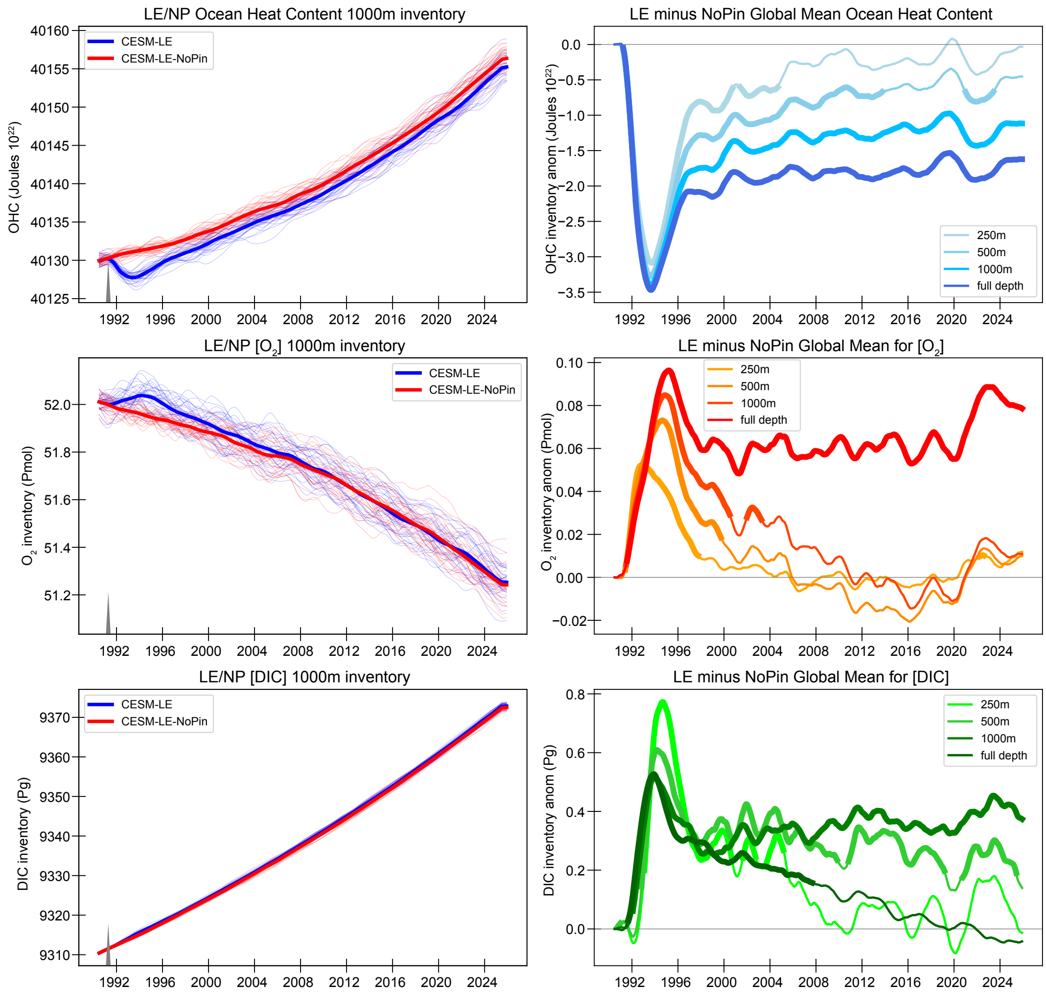

Figure S2. Left column: CESM-LE (blue) and CESM-LE-NoPin (red) individual members (thin lines) and ensemble mean (thick line) time series for global mean Ocean Heat Content (blue, Joules 10^{22}), Oxygen inventory (orange, Pmol), and Dissolved Inorganic Carbon inventory (green, Pg) for top 1000m for full model time series (1990-2025). Right column: CESM-LE minus CESM-LE-NoPin inventory difference for each variable with thicker line indicating significant difference between two ensembles at 2σ Deser:2012a. Inventory plots include lines for depths 250m, 500m, 1000m and full depth. Time series are seasonally detrended, smoothed with a 12-month running mean. Gray triangle marks timing of eruption.

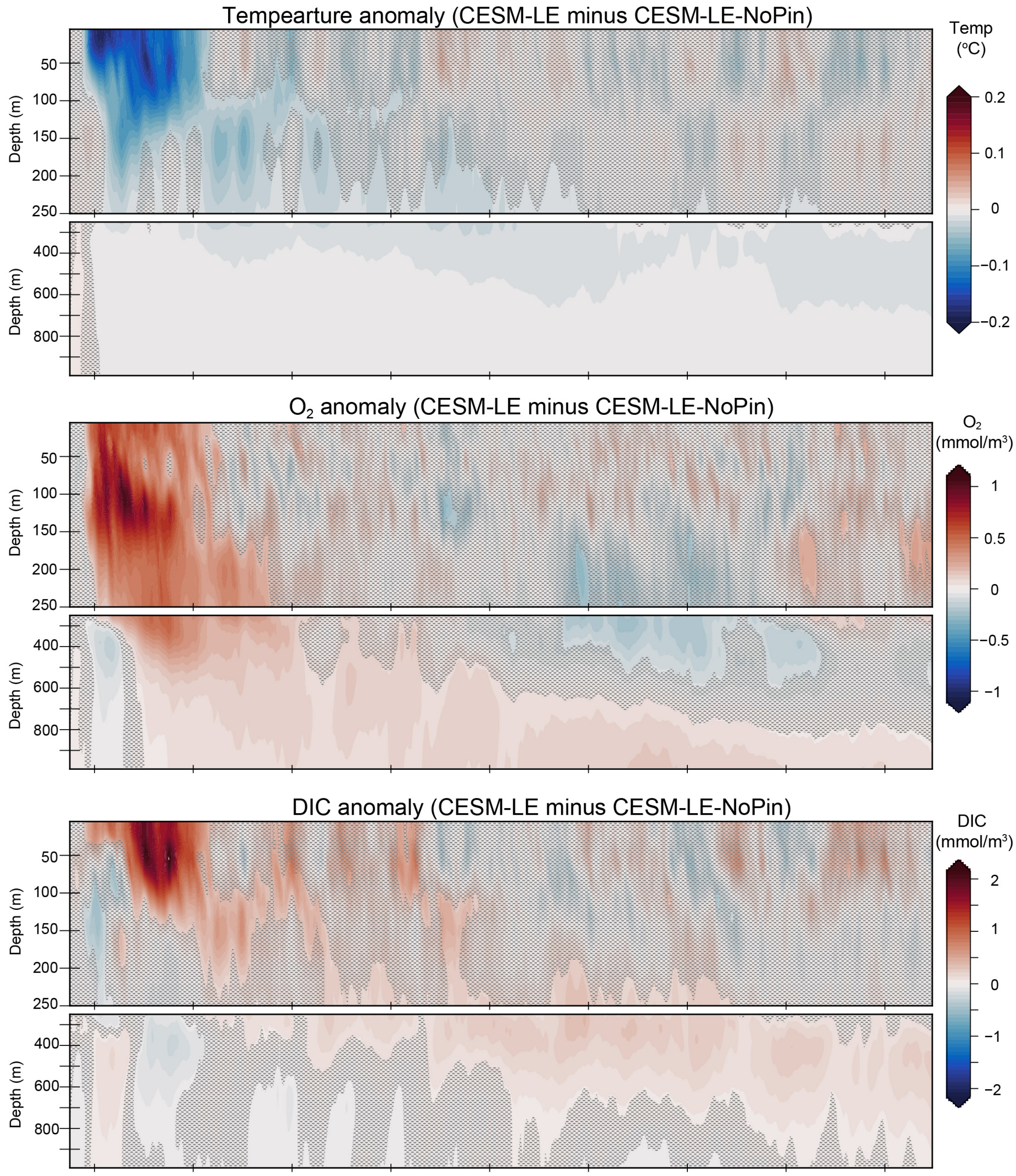

Figure S3. Globally averaged vertical profile of difference plots (CESM-LE minus CESM-LE-NoPin) for ensemble mean in a) temperature (°C) b) [O_2] (mmol/m^3), and c) [DIC] (mmol/mm^3) for full model time period (1990-2025). Stippling indicates time/depth where differences are not significant at the 95% confidence level Deser:2012a. Positive anomalies (warm colors) indicate greater values with the eruption of Pinatubo while negative anomalies (cool colors) indicate lower values with the eruption.

June 30, 2022, 3:52pm

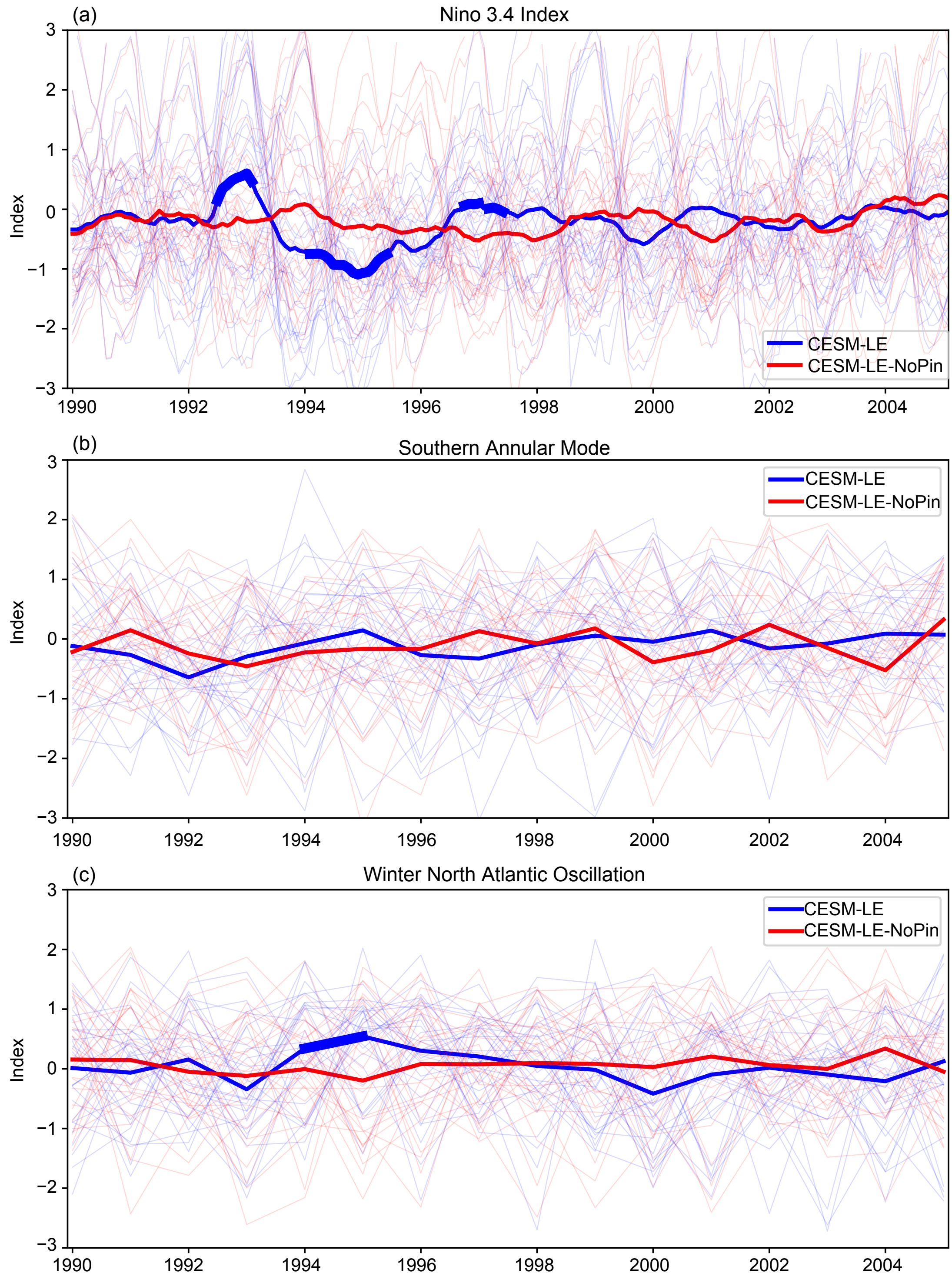

Figure S4. CESM-LE (blue) and CESM-LE-NoPin (red) individual members (thin lines) and ensemble mean (thick line) time series of pertinent climate indices: (a) monthly mean Niño 3.4 index (b) Southern Annual Mode (SAM), and (c) winter (DJF) North Atlantic Oscillation (NAO). Thicker line segments on ensemble means indicate significant difference between two ensembles at 2σ Deser:2012a.

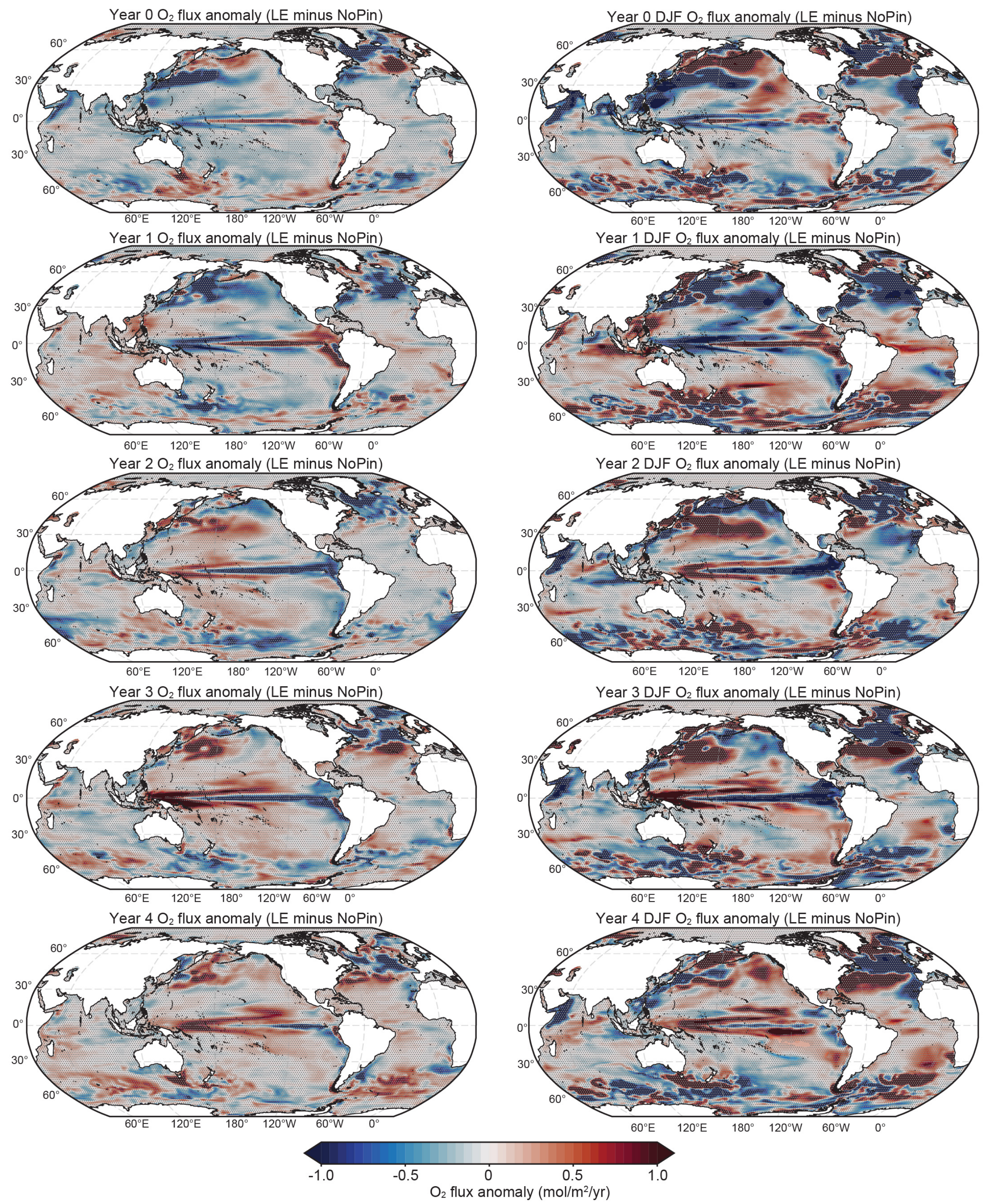

Figure S5. Evolution of annual mean anomalies (CESM-LE minus CESM-LE-NoPin) of oxygen fluxes during the first five years following the June 1991 eruption of Pinatubo: Year 0 (July 1991-June 1992), Year 1 (July 1992-June 1993); Year 2 (July 1993-June 1994); Year 3 (July 1994-June 1995); Year 4 (July 1995-June 1996). Anomalies are calculated by removing the seasonal cycle and annually averaging over respective months. Positive flux anomalies (warm colors) indicate increased efflux of O_2 in ocean efflux regions or less uptake with the eruption of Pinatubo. Negative flux anomalies (cool colors) indicate less efflux or increased uptake with the eruption of Pinatubo. Stippling indicates areas without significant difference between the two

June 30, 2022, 3:52pm

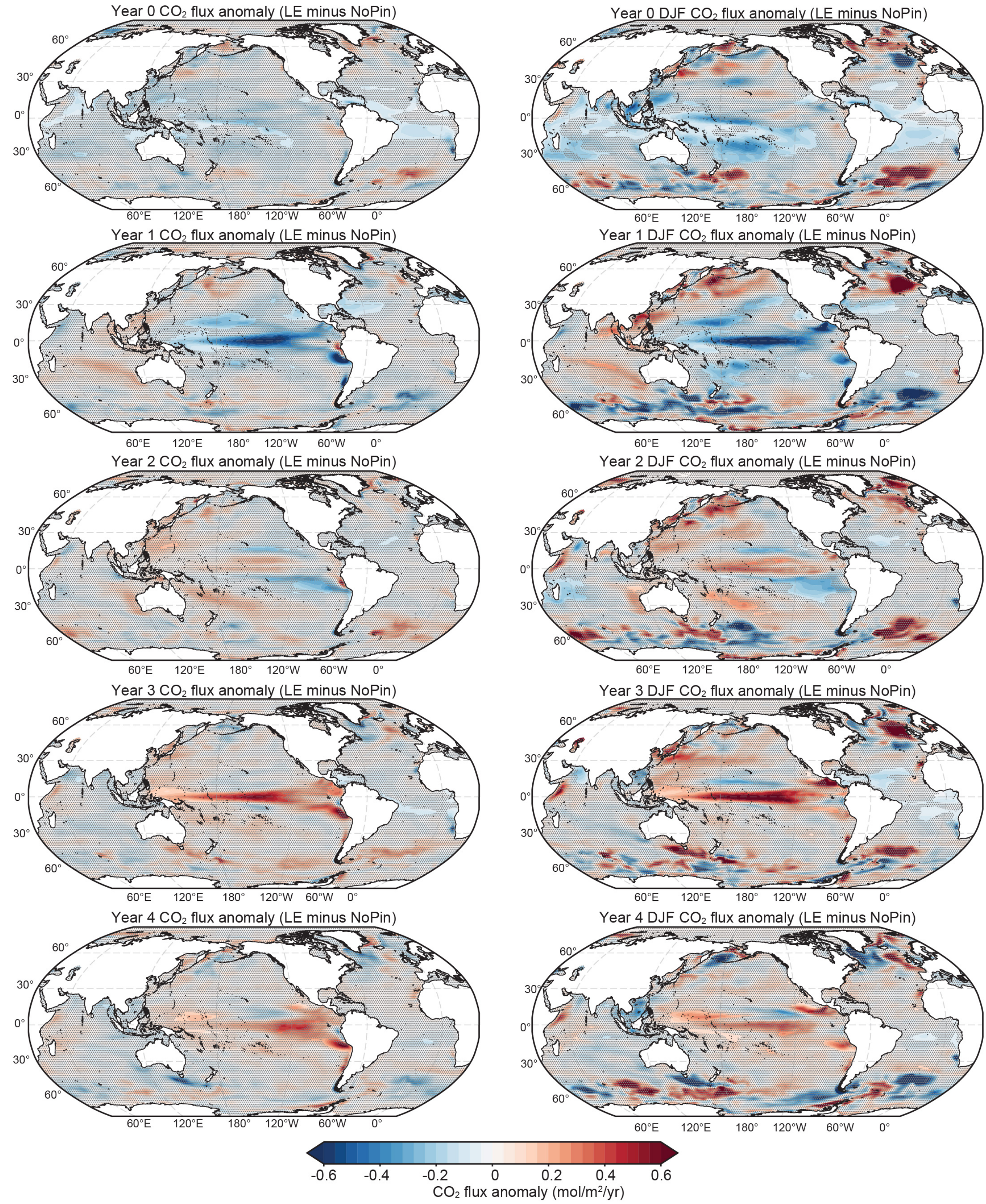

Figure S6. Evolution of annual mean anomalies (CESM-LE minus CESM-LE-NoPin) of carbon fluxes during the first five years following the June 1991 eruption of Pinatubo: Year 0 (July 1991-June 1992), Year 1 (July 1992-June 1993); Year 2 (July 1993-June 1994); Year 3 (July 1994-June 1995); Year 4 (July 1995-June 1996). Anomalies are calculated by removing the seasonal cycle and annually averaging over respective months. Positive flux anomalies (warm colors) indicate increased efflux of CO_2 in ocean efflux regions (e.g. equatorial Pacific) or less uptake with the eruption of Pinatubo. Negative flux anomalies (cool colors) indicate less efflux or increased uptake with the eruption of Pinatubo. Stippling indicates areas without significant

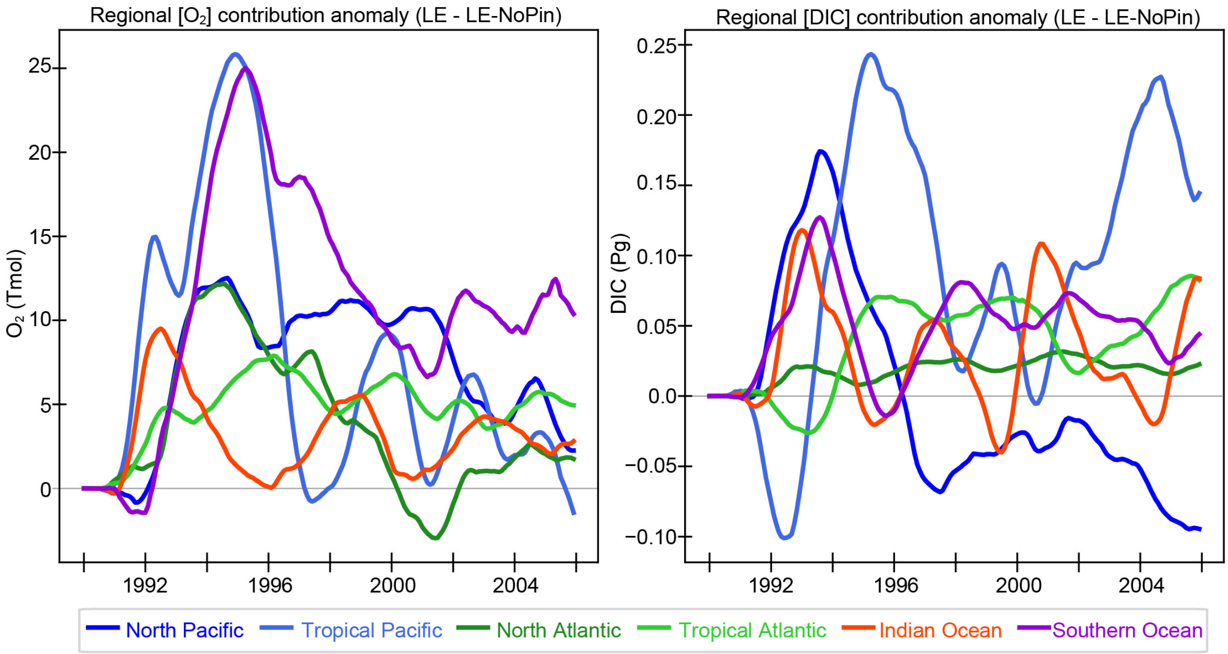

Figure S7. Regional contributions to O_2 (left) and DIC (right) 1000m concentrations anomalies (CESM-LE minus CESM-LE-NoPin). Ensemble mean time series, with 12-month running mean, for the North Pacific and Atlantic (¿30°N), Tropical Pacific and Atlantic (30°N - 30°S), Indian Ocean, and Southern Ocean. Can be compared to global values in Figure 2b.

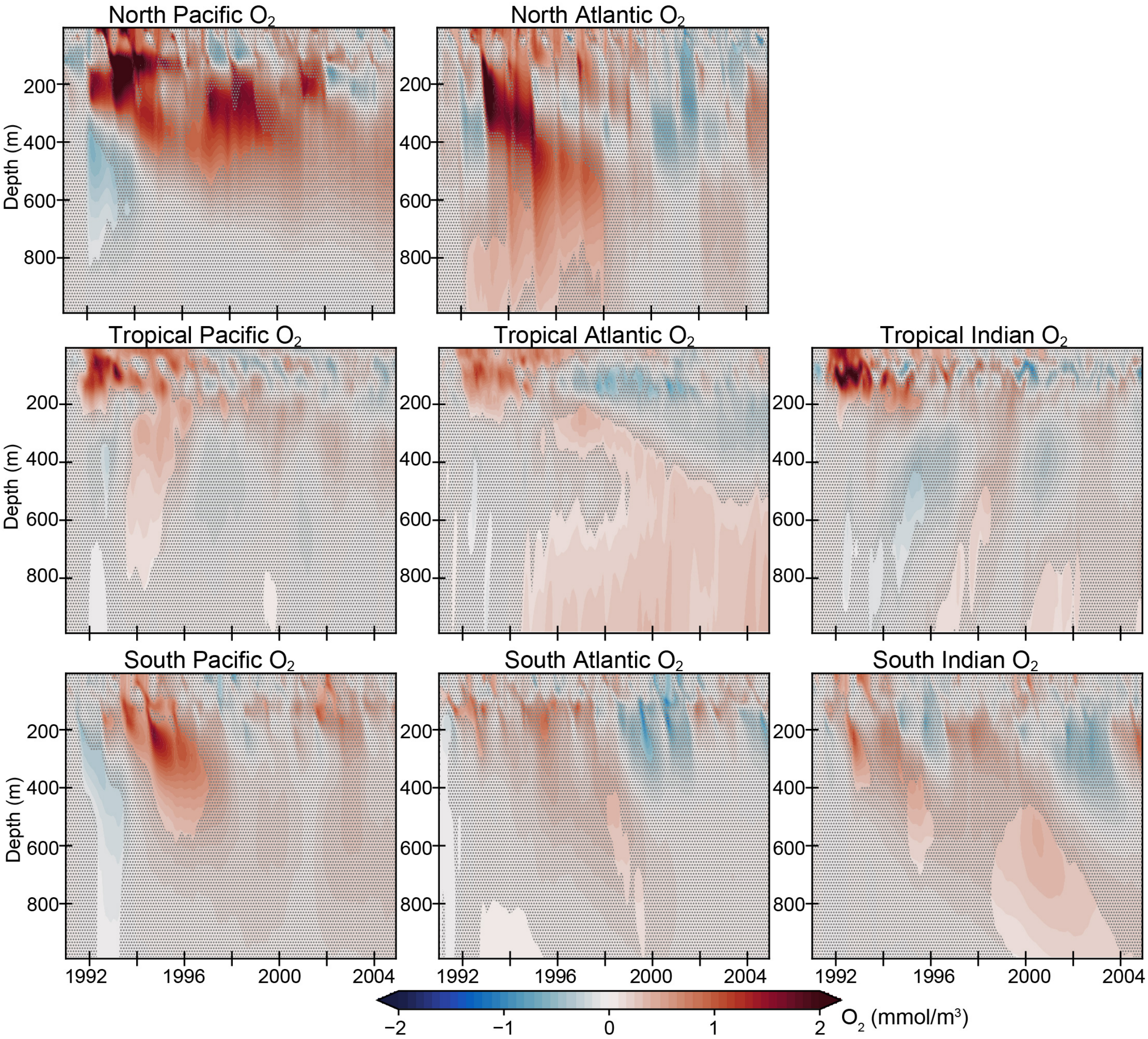

Figure S8. Regionally averaged vertical profile of difference (CESM-LE minus CESM-LE-NoPin) plots for ensemble mean O_2 inventory (mmol/m^3) for full model time period (1990-2025). Separations are made for the Pacific, Atlantic, and Indian basins into northern (¿30°N), tropical (30°N-30°S), and southern sections (¡30°S). Stippling indicates time/depth where differences are not significant at the 95% confidence level Deser:2012a. Positive anomalies (warm colors) indicate greater oxygen inventory values with the eruption of Pinatubo while negative anomalies (cool colors) indicate lower oxygen with the eruption.

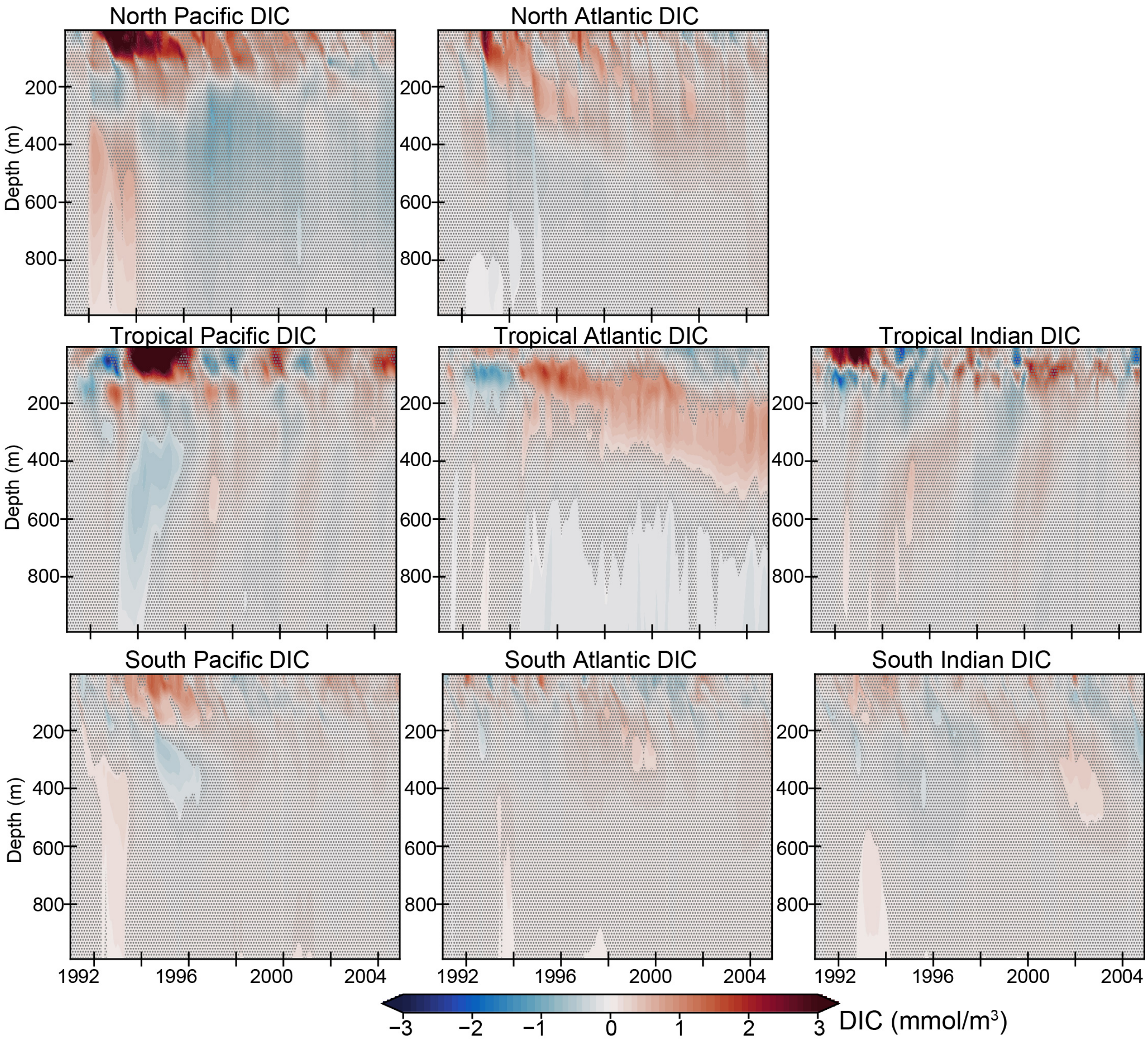

Figure S9. Regionally averaged vertical profile of difference (CESM-LE minus CESM-LE-NoPin) plots for ensemble mean DIC inventory (mmol/m^3) for full model time period (1990-2025). Separations are made for the Pacific, Atlantic, and Indian basins into northern (¿30°N), tropical (30°N-30°S), and southern sections (¡30°S). Stippling indicates time/depth where differences are not significant at the 95% confidence level Deser:2012a. Positive anomalies (warm colors) indicate greater DIC inventory values with the eruption of Pinatubo while negative anomalies (cool colors) indicate lower DIC levels with the eruption.

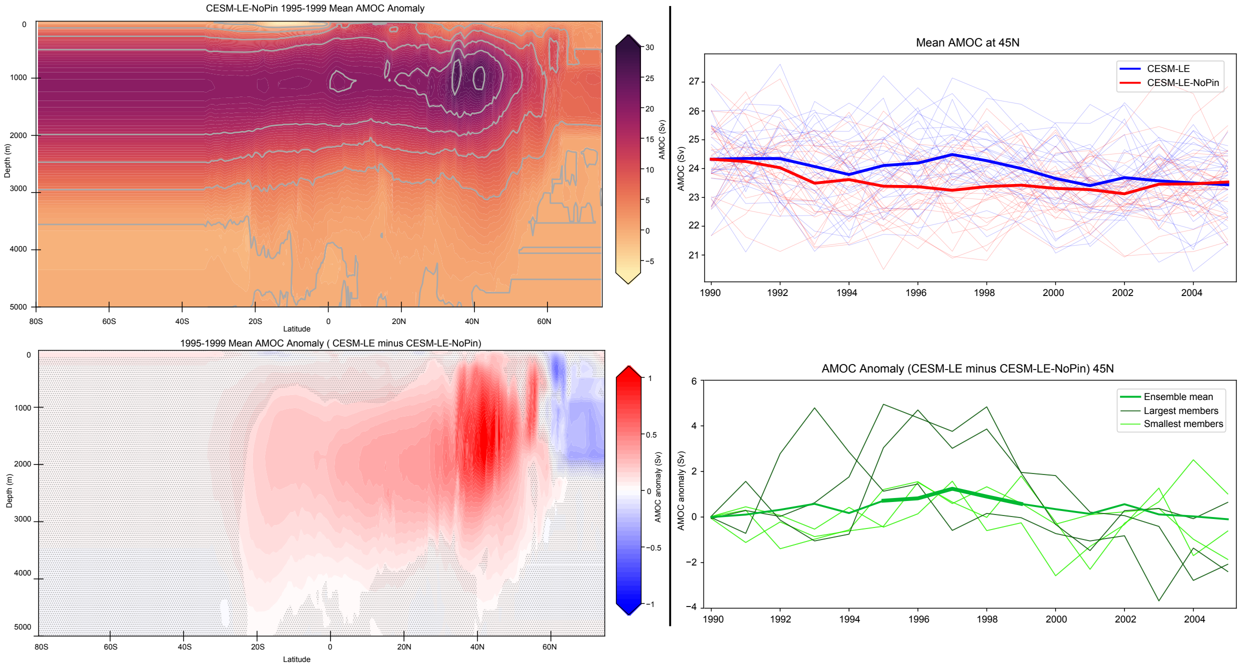

Figure S10. Time-mean Atlantic Meridional Overturning Circulation (AMOC) from (a) the "control" CESM-LE-NoPin ensemble mean (yrs 1995-99 mean) and (b) CESM-LE minus CESM-LE-NoPin ensemble mean anomaly (yrs 1995-99 mean). The contour interval in (a) is 5 Sv. Stippling on (b) indicates depth/latitude where ensemble mean differences are not significant at the 95% confidence level Deser:2012a. Positive anomalies (warm colors) indicate stronger AMOC values with the eruption of Pinatubo while negative anomalies (cool colors) indicate weaker AMOC values with the eruption. (c) shows a time series of the maximum AMOC at 45°N in CESM-LE (blue) and CESM-LE-NoPin (red) individual members (thin lines) and ensemble mean (thick lines). CESM-LE minus CESM-LE-NoPin anomalies (d) for the ensemble mean (thick line) along with individual ensembles representing the three largest (dark green thin lines) and three smallest (light green thin lines) changes for the time period. Thicker line segments on ensemble means (d) indicate significant difference between two ensembles at 2σ Deser:2012a.

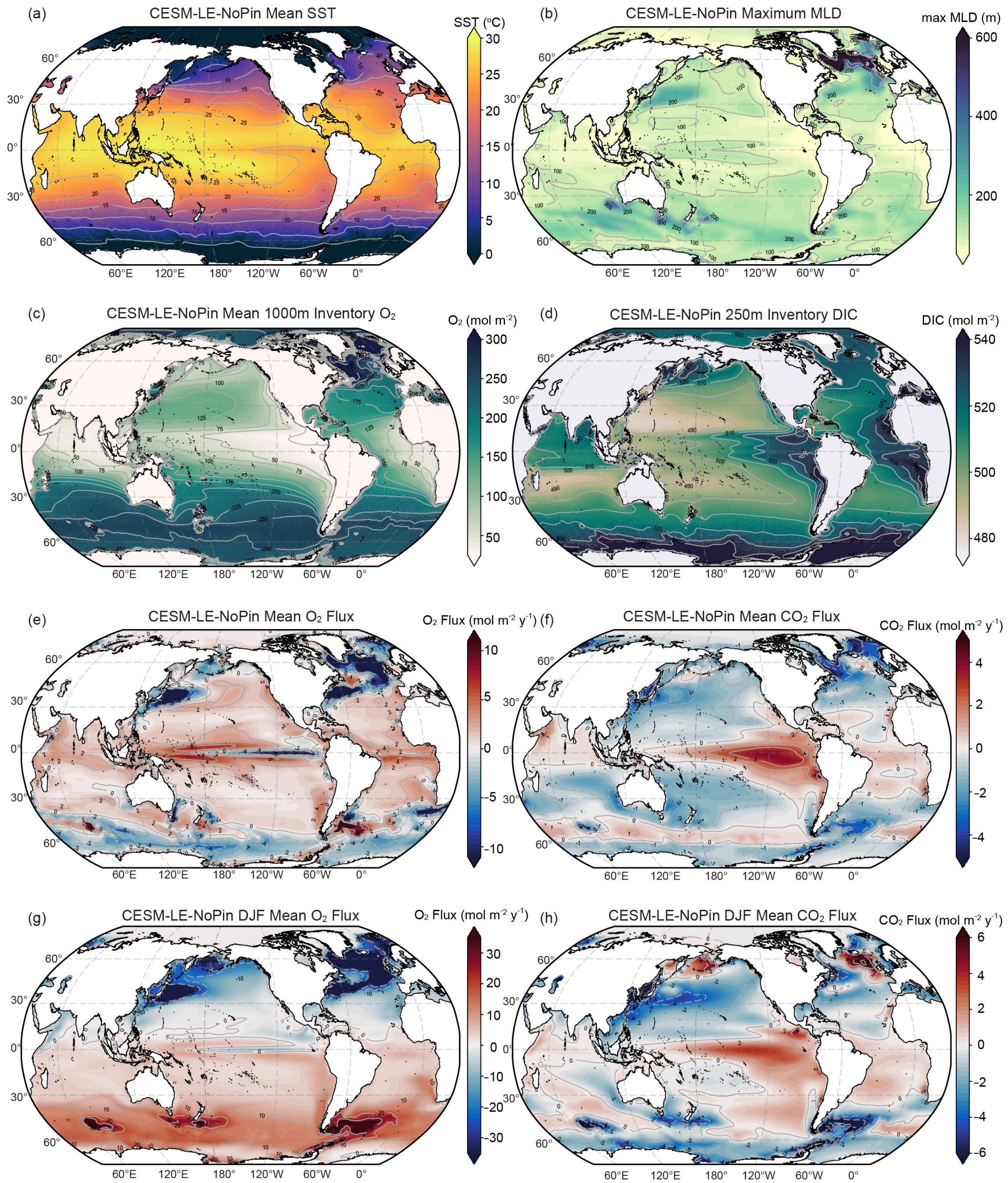

Figure S11. Mean state maps of 1990s CESM-LE-NoPin ensemble mean for (a) SST (contour interval 5°) , (b) maximum MLD (contour interval 100m) (c) 1000m O_2 inventory (contour interval 25 mol/m^2) , (d) 250m DIC inventory (contour interval 10 mol/m^2), (e) O_2 flux (contour interval 2 mol/m^2/yr), (f) CO_2 flux (contour interval 1 mol/m^2/yr), (g) DJF O_2 flux (contour interval 10 mol/m^2/yr), (h) DJF CO_2 flux (contour interval 2 mol/m^2/yr).